이학박사 학위논문

Highly Controlled Synthesis of Au-Ag Head-Body Nanostructures and Study of Their Geometry-dependent Optical Properties

고도로 제어된 금-은 헤드부-바디부로 구성된 나노구조체의 합성과 구조에 따른 플라즈모닉 특성 연구

2018 년 8 월

서울대학교 대학원

화학부 무기화학

유 명 화

Highly Controlled Synthesis of Au-Ag Head-Body Nanostructures and Study of Their Geometry-dependent Optical Properties

고도로 제어된 금-은 헤드부-바디부로 구성된 나노구조체의 합성과 구조에 따른 플라즈모닉 특성 연구

지도교수 남 좌 민

이 논문을 이학박사 학위논문으로 제출함

2018 년 8 월

서울대학교 대학원

화학부 무기화학

유 명 화

유명화의 박사 학위논문을 인준함

2018 년 8월

위 원 장 손 병 혁 (인)

부위원장 홍 병 희 (인)

위 원 김 지 환 (인)

위 원 이 광 렬 (인)

위 원 남 좌 민 (인)

Abstract

Highly Controlled Synthesis of Au–Ag Head–Body Nanostructures and Study of Their Geometry–dependent Optical Properties

Myung–Hwa You

Department of Chemistry

The Graduate School

Seoul National University

Noble metal nanoparticles (Au, Ag or Cu) have been extensively exploited due to their unique applications in various fields that range from optics, electronics, energy conversion to biomedicine. Most of fascinating properties of noble metal nanoparticles come from localized surface plasmon resonances (LSPR) which is a coherent collective oscillation of electrons in a conduction band excited by the oscillating electric field of the incident light. The resonance frequency LSPs are highly dependent on the size, shape, composition of nanoparticles, small changes in interparticle distance and dielectric environment. Therefore, designing and synthetic strategies of

plasmonic nanostructures allow us to manipulate, enhance and utilize the various properties. Recently, the full potential of plasmonic nanoparticles has been expanded from single component which has monotonic and confined properties to bi- or multiple component in forming and utilizing its structure and applications. Compared to single component nanoparticles, bimetallic nanoparticles can generate more diverse and new properties, emerging from integration and synergistic interactions of physical and chemical properties of individual component in combined system. Especially, bimetallic nanoparticles can enhance the optical signals such as Raman scattering or fluorescence depending on the internal structures in a similar way to the pair of nanoparticles separated in a nanometer distance. The important geometric factor to enhance such an optical signal is internal nanocrevices or deliberately formed nanogap structures by amplifying electromagnetic fields at hot-spot regions. Particularly, formation of sharp nanocrevice or narrow gap around 1 nm is significant to facilitate and enhance the effective plasmonic coupling. Among the various kinds of bimetallic nanostructures, plasmonic structures, asymmetrically connected through a conductive junction can support diverse plasmon modes which can be explained by plasmon hybridization model. The symmetry breaking in size or composition of the nanoparticle and following incomplete cancellation of charges support exceptional antibonding plasmon mode, accompanying a bonding plasmon mode. However, it is highly challenging to synthesize plasmonic bimetallic nanostructures with a delicate structural control, and high reproducibility as the energy level is not preferred in a

thermodynamics point of view. Especially, controlling the sharpness, thickness and width of conductive junction in bimetallic nanostructures enables us to control the optical, and electrical characteristics of bimetallic material, so that fundamental understanding of synthetic mechanism and developing the controlling methods should be emphasized.

In this thesis, various nanostructures possessing a conductive junction has been designed and synthesized by utilizing DNA-based synthetic strategies. Especially, Au-Ag head-body structures with highly controllable conductive junctions and resulting plasmonic properties depending on their geometries will be introduced. In the synthesis, DNA based-kinetic control enabled the anisotropic growth of secondary metal (Ag) on the Au surface under the appropriate concentration of reducing agent, precursor, salt and pH value in a combinatory manner. Hence, these kinetics factors tailor the final morphologies of Ag body structures in Au-Ag head-body into a sphere, plate, truncated right bipyramid or bar, accompanying diverse junction geometries with different length and thickness. Through the fine control of the conductive junction, we could investigate the relationships in structural changes, EM field enhancement and signal amplification. This highly precise and controllable synthesis is expected to open revenues and provide new insights for plasmonic nanostructures which can be applied in variety of fields.

The 1st chapter of the thesis introduce a synthetic method and optical properties of Au-Ag head-body nanosnowman structures with structural controllability of sharpness of conductive junction. Here, NaCl as a salt and DNA-based synthetic strategies allow us to manipulate the various asymmetric Au-Ag nanosnowman structures and studied their plasmon modes cover from visible to near-infrared range. It was shown that change in the plasmonic neck within a nanosnowman structure introduce various plasmon modes such as charge-transfer and capacitive plasmon modes and dramatically affects the resulting electromagnetic field and optical signal. The strongest electromagnetic field was observed in the crevice area on the junction and synthesizing a thinner and sharper neck junction is critical to generate the stronger electromagnetic field in the crevice area and to obtain the charge-transfer mode-based near-infrared signal. As a result, highly reproducible SERS signals can be generated from these nanosnowman structures with a linear dependence on particle concentration (5 fM to 1 pM) and the SERS-enhancement factor values of >108 can be obtained with the aid of resonance effect in SERS.

In the 2nd chapter describes the noble synthetic method to synthesize various silver body structures in Au-Ag head-body structures as plate (PL), truncated right bipyramid (RBP) and bar (B) structures based on DNA-modified gold nanocubes as a seed. In synthetic scheme, DNA was a critical parameter which induce stacking faults and various morphologies in silver body during the growth. Depending on carefully controlled kinetic condition, density of stacking faults, growth direction and final morphologies of silver were decided. Further, I investigated plasmonic properties of Au−cube Ag−body structures with various conductive junction as thick and short or thin and long geometry by controlling DNA sequence, concentration of reducing agent and polymers. Specially, we observed distinct charge−transfer plasmon modes in Au−cube Ag−RBP structures which has ~ 20 nm width and ~ 1.5 nm length of conductive junction. Meanwhile, negligible development of charge−transfer plasmon mode was observed in Au−cube Ag−Bar structures which has each of ~10 nm width and length of conductive junction. These delicate control in conductive junction and accompanying optical properties can allow us to indirectly monitor the electronic properties in 10 to 20 nm regime.

Keywords: Plasmonics, Bimetallic Structures, Anisotropy, Nanosnowman, Head−Body Structures, Connected Dimer, Nanoantenna, Charge−transfer Plasmon Mode, Bonding Dipolar Plasmon Mode, Capacitive Coupling, Conductive Junction, Conductance, Surface−Enhanced Raman Scattering (SERS)

Student Number : 2012−23047

Contents

Abstract ········· i
Contents ········· vi
List of Figures ········· viii

Chapter 1. Plasmonic Nanosnowmen with a Conductive Junction as Highly Tunable Nanoantenna Structures and Sensitive, Quantitative and Multiplexable Surface-Enhanced Raman Scattering Probes

1.1. Introduction ········· 2
1.2. Experimental Section ········· 6
  1.2.1. Materials ········· 6
  1.2.2. Methods ········· 6
1.3. Results and Discussion ········· 12
1.4. Conclusions ········· 29
1.5. References ········· 31
Figures ········· 37

Chapter 2. Kinetically Controlled Structures and Stacking Faults of Silver Body in Au(cube)-Ag Head-Body Nanostructures with Conductive Junction and its Optical Properties

2.1. Introduction ·· 44
2.2. Experimental Section ·· 49
2.3. Results and Discussion ·· 51
2.4. Conclusions ·· 64
2.5. References ··· 66
Figures ··· 70

Abstract (in Korean) ·· 76

List of Figures

Chapter 1. Plasmonic Nanosnowmen with a Conductive Junction as Highly Tunable Nanoantenna Structures and Sensitive, Quantitative and Multiplexable Surface−Enhanced Raman Scattering Probes

Figure 1.1. (A) Schematic, calculated electromagnetic field views and transmission electron microscope images of various Au−Ag head−body nanosnowman structures with various neck junction morphologies. Panels 1−3 for 40 nm Au−55 nm Ag head−body nanosnowmen at 10 mM, 3 mM and 0.7 mM salt concentrations, respectively. (B) Schematic and TEM images of Au−Ag head−body nanosnowman structures with different Ag body sizes. Panels i−iii for the snowmen with 40 nm Au head and 30, 40, and 65 nm Ag bodies, respectively. All the scale bars are 100 nm in the TEM images (the scale bars in the inset images are 20 nm).

Figure 1.2. (A) The UV−vis extinction spectra of the Au−Ag head−body nanosnowmen with 40 nm Au head and 55 nm Ag body that correspond to the structural changes at different salt concentrations −10 mM NaCl (1, indistinct neck), 3, 2, and 1.5 mM NaCl (2, 2′ and 2″ , thick neck), and 0.7 mM NaCl (3, thin neck). (B) The extinction spectra of Au−Ag head−body nanosnowmen with 40 nm Au head and different Ag body sizes. (C) The deconvoluted extinction spectra from Figure 2A (0.7 mM NaCl − 3, thin neck) with five−parameter Lorentz fitting.

Figure 1.3. Nanosnowman structure-based change in electromagnetic field and SERS signal. Conductive neck junction morphology-based change (A) and Ag body size-based change (B) in the SERS signal intensity at 1325 cm−1 with varying excitation laser wavelengths. The numbered boxes in panel A correspond to structures 1, 2, and 3 in Figure 1A. (C) The 3D FEM calculation-based electromagnetic field enhancements and distributions with different plasmonic neck morphologies at 514, 633, 785, and 1005 nm excitation wavelengths. The small arrows indicate the directions of the calculated electric field and the accompanying illustrations on the bottom of each simulation image show the charge distributions. (D) SERS spectra of FAM dyes on 40 nm Au−55 nm Ag head-body nanosnowmen from 10 mM NaCl (indistinct neck), 3 mM NaCl (thick neck), and 0.7 mM NaCl (thin neck) concentrations at 633 nm excitation wavelength. All the spectra in these figures were taken with ~10 mW laser power, 3 s acquisition time, 20× objective lens, and 72 pM particle concentration.

Figure 1.4. Comparison in the SERS intensities between different Raman dyes with the nanosnowman structure with a thin neck junction (structure 3) at 514, 633, and 785 nm laser wavelengths. All the spectra were taken with ~10 mW laser power, 10 s acquisition time, 20× objective lens, and static mode.

Figure 1.5. Nanosnowman concentration-dependent change in SERS intensity. (A) SERS intensity plot at 1325 cm−1 of FAM dye from Au− Ag head-body nanosnowmen in Figure 1A-3 as

a function of nanoparticle concentration at three different excitation laser wavelengths (~10 mW laser power, 3 s acquisition time, and 20× objective lens.) (B) SERRS intensity plot at 1195 cm−1 of Cy5 Raman dye from same particles as a function of particle concentration at 633 nm excitation laser wavelength (~10 mW laser power, 10 s acquisition time, and 20× objective lens).

Figure 1.6. The representative surface-enhanced resonance Raman scattering (SERRS) spectra of ORG, Cy3, Cy5, Alexa 546, Alexa 647 and Alexa 750 Raman dyes on the nanosnowmen with 40-nm AuNP head and 55-nm AgNP body at the resonance excitation laser wavelengths.

Chapter 2. Kinetically Controlled Structures and Stacking Faults of 2nd Body in Au(cube)-Ag Head-Body Nanostructures with Conductive Junction and its Optical Properties

Figure 2.1. Illustration of scheme for synthesizing various types of Au-Ag hetero dimer structures and transmission electron microscope images of Aucube-Ag;plate, truncated right bipyramid and bar head-body structures with controlled conductive junction morphologies in various synthetic conditions.

Figure 2.2. (A) Transmission electron microscope image of GC-STRB structures with low magnitude image. (B) Orientation dependent HAADF-TEM images of GC-STRB from front and

lateral view and corresponding FFT patterns marked as box.

Figure 2.3. (A) Transmission electron microscope image of GC−SB structures with low magnitude image. (B) Representative single−particle HAADF−TEM images of GC−SB and magnified lattice image in silver body and corresponding FFT patterns from marked as box 1.

Figure 2.4. (A) The time−dependent UV−vis extinction spectra of the GC−STRB with continuous development in bonding dipolar plasmon mode and charge−transfer plasmon mode. (B) The time dependent UV−vis extinction spectra of GC−SB with negligible development in both bonding dipolar plasmon mode and charge−transfer plasmon mode.

Figure 2.5. (A) The 3D FEM calculation−based extinction spectra of GC−STRB (thick and short junction, inset) structures with different conductive junction geometries (B) The 3D FEM calculation−based extinction spectra of GC−SB (thin and long junction, inset) structures with different conductive junction geometries.

Figure 2.6. (A) TEM images of GC−STRB structures with different Ag body sizes. All the scale bars are 50 nm in the TEM images. (B) The extinction spectra of GC−STRB structures

with different Ag body sizes. (C) Comparison in the SERS intensities between different sizes in GC−STRB structures. (D) Comparison in the SERS intensities between Raman dye modified GC (control) GC−STRB and GC−SB structures. (E) SERS intensity plot at 1198 cm^{-1} of Cy3 dye from GC−STRB structures in Figure 2 as a function of nanoparticle concentration. All the spectra were taken at 633 nm laser with ~3.3 mW laser.

Chapter 1

Plasmonic Nanosnowmen with a Conductive Junction as Highly Tunable Nanoantenna Structures and Sensitive, Quantitative and Multiplexable Surface-Enhanced Raman Scattering Probes

1.1. Introduction

The localized surface plasmon resonance (LSPR) can be excited by a broad range of incident light from visible to near IR range, and the LSPR−governed optical response of individual nanoparticles is strongly dependent on their size, shape, composition, and small changes in interparticle distance, junction structure, surface modification, and solvent[1−12]. This structure and environment−dependent LSPR has been used to enhance optical signals such as Raman scattering and fluorescence in a wide range of research fields from optics to biomedical applications[1,2,4,5,8−10,13,14]. A major optical signal amplification source is the amplified electromagnetic (EM) field at the junction area formed between nanoparticles (e.g., single protein−tethered dimers[14] and single DNA−tethered nanodumbells[1,2,9]) or the interior gap within a single nanoparticle[1−4,9,10,14−22]. Different geometric configurations can induce distinct spectral features, and thus multimeric plasmonic nanostructures can serve as a highly sensitive nanoantenna with specific polarization directions varying by the size and position of each particle with respect to each other[20,22−27]. These geometric factors affect the polarization direction and magnitude of plasmonic coupling and the SERS signal intensity. Therefore, understanding and controlling LSPR modes is the fundamental basis for the use of these nanoantenna structures. In a simple plasmonic dimer structure with a gap,[1,2,9,14,22] a redshift of longitudinal plasmon-mode peak is typically observed as the interparticle distance decreases due to the strong plasmonic coupling, and the EM field intensity increases while the interparticle gap decreases until quantum tunneling effect becomes dominant for <0.5 nm gap[2,28-30]. Recent results further show that more diverse plasmon modes exist in the heterodimeric structures than homodimeric structures due to the symmetry breaking of plasmon modes and more diverse plasmon coupling modes. In some cases, much stronger EM field and surface-enhanced Raman scattering (SERS) can be generated using these broken-symmetry structures[7,31-33]. Although various synthetic and fabrication methods for these structures have been proposed,[2,12,21,34-38] tuning nanometer or sub-nanometer structural change and structure-dependent optical properties with nanometer-sized plasmonic gap in a high precision and yield is challenging and of interest for more general and wider use of plasmonic nanostructures and SERS nanoprobes. It should be also noted that the interparticle gap in solution can be fluctuating and interparticle gap junction can be largely varied from particle to particle. Recently, it has been reported that new longitudinal plasmon modes can be generated when interparticle separation is reduced to zero in a dimer, and these plasmon modes are blue shifted as particle overlap is further increased.[13,28,39,40] In the plasmonic dimers with an interparticle gap, it is not physically possible to have a purely positive or negative charge on each particle. This unconventional mode with a net charge of each particle in a fused dimeric structure, however, becomes possible by forming a conductive contact between particles due to the charge transfer through a conductive junction. Interestingly, a sharp plasmonic junction region between two particles can generate the strong EM field.20,39,40 Despite these interesting properties of overlapping dimers, there have not been enough experimental studies on these structures and the precise and reliable synthetic methods for these types nanostructures have not been readily available for these studies. Further, it would be beneficial to combine two different metals within a single nanostructure in a controllable fashion because of their newly resulting and useful optical and chemical properties, including direct electron transfer, tunable and intense plasmonic optical properties, higher chemical affinity, or increased catalytic activity[3,41−46]. Herein, we designed and synthesized the anisotropic Au−Ag head−body nanosnowman structures with various plasmon modes including charge−transfer plasmon (CTP and capacitive coupling modes in a structurally controllable and reproducible manner. The composition, shape, size, and charge−transfer junction−

dependent plasmonic properties and SERS signals of the plasmonic nanosnowmen were explored and analyzed. In particular, we demonstrated that the sharp plasmonic neck region between Au head and Ag body in the snowman structure is a key to the generation of stronger LSPR and SERS signals.

The correlations between excitation laser source, Raman dye type and plasmonic nanosnowman structure were studied, and it was shown that the nanosnowman structures are excellent platforms for highly sensitive, quantitative and multiplexable SERS applications.

.

1.2. Experimental Section

1.2.1. Materials

All the chemical reagents [AgNO3, polyvinylpyrrolidone (MW 40,000), (+)-sodium Lascorbate] were purchased from the Sigma-Aldrich (St. Louis, MO, USA) and used without further purification. Au nanoparticles (AuNPs) were purchased from Ted Pella, Inc. (Redding, CA, USA). HPLC-purified oligonucleotides and NAP-5 column were purchased from IDT, Inc.(Coralville, IA, USA) and GE Healthcare (Sephadex G-25 medium, DNA grade), respectively. NANO pure water (>18.0 MΩ, Milli-Q) was used for all the experiments. The formvar/carboncoated copper grid (Ted Pella, Inc. Redding, CA, USA) and TEM (JEM-2100, JEOL, Japan, 200 kV, from National Center for Inter-University Research Facilities at Seoul National University) were used for the TEM analysis.

1.2.2. Methods

Preparation of DNA-modified AuNPs. The modification of DNA on AuNPs was based on literature procedures.1-4 Oligonucleotides were reduced by dithiothreitol (DTT, 0.1 M) in phosphate-buffered saline solution (0.17 M, pH = 8.0) and then purified using a desalting

NAP-5 column. For the preparation of DNA-modified AuNPs, purified DNA [5'-CACGCGTTTCTCAAA-(PEG)6-A10-(Raman dyes)-(CH2)3-SH-3'] were used to conjugate on AuNPs. The loading number of DNA was determined based on the fluorescence analysis. DNA modified AuNPs were mixed with 0.1M KCN for 10 min. The loading numbers of DNA per particle were determined to be ~400, 800 and 1,800 strands for 40, 50 and 60 nm AuNPs, respectively. The excess amount of DNA (80 fold for FAM, ORG, Alexa546, Alexa647 and Alexa750 Raman dye cases and 50 fold for Cy3 and Cy5 cases) were added for DNA modification process. Briefly, for FAM Raman dye-modified DNA, 387 μL of 44.9 μM DNA solution was mixed in 4.5 ml of 0.1 nM 40-nm AuNP solution. The mixture was adjusted to obtain a final phosphate concentration of 10 mM (pH 7.4) with 100 mM phosphate buffer. The resulting solution was wrapped in an aluminum foil and placed on an orbital shaker at room temperature for 30 min. Next, the resulting solution was adjusted to 0.3 M NaCl (0.05 M × 2 and 0.1 M × 2) by the addition of salting buffer (2 M NaCl in 10 mM PB) every 20 min and heated for 5 min in a water bath at 70 ºC after each step to minimize the interactions between DNA bases and gold surface. After the salt-aging process, the solution was incubated overnight in an orbital shaker at room temperature. The solution was then centrifuged

(12,000 rpm for 40-nm AuNPs, 10,000 rpm for 50-nm AuNPs and 8000 rpm for 60-nm AuNPs) for 10 min, respectively,
and the supernatant was removed carefully to get rid of unmodified DNA and unreacted reagents. The precipitate was redispersed in 10 mM PB solution (pH 7.4; this procedure was repeated four times). For example, when 1 mL of DNA-modified solution was centrifuged under this condition, <10 μL of solution with precipitates was remained after the supernatant was removed and redispersed in 10 mM PB of 1,000 μL. As a result, the final concentration of salt was adjusted to <1 nM after repeated washing processes (4 times). Finally, the precipitate was redispersed in a desired PBS solution to adjust NaCl concentration (10 mM PB, pH 7.4). These DNA modified AuNPs were used as seeds for an asymmetric Ag body growth. The concentration of DNAmodified
AuNPs was characterized using the UV-Vis spectrophotometer (Agilent 8453 spectrophotometer, USA).

Synthesis of Au-Ag head-body nanosnowmen.

2% polyvinylpyrrolidone (PVP), 0.1 M L-sodium ascorbate (L-SA) and 1 mM silver nitrate in deionized water were used. DNA-modified 40-nm AuNPs were used as the seeds for the asymmetric growth of an AgNP on DNA-AuNPs. The molar ratio between the number of

PVP repeating units and Ag+ (PVP/Ag+) was kept at 100 (the source for Ag+ is AgNO3), and the molar ratio between the reductant and Ag+ (L-SA/Ag+) was kept at 50. To control the extent of the overlap between Au and Ag nanoparticles in forming a plasmonic neck region, various salt concentrations from 300 mM to 0.3 mM were used. Typically for 55 nm Ag body, 200 μL of 70 pM DNA-modified 40-nm AuNP solution with different salt concentrations (300 mM, 10 mM, 3 mM, 2 mM, 1.5 mM or 0.7 mM) was reacted with 65.1 μL of 1 mM AgNO3 solution in the presence of 36.2 μL of 2% PVP and 32.6 μL of 0.1 M L-SA, respectively. The resulting mixture was mildly pipetted for several minutes until solution color starts to change and kept in an orbital shaker at room temperature. The reaction time was increased from 5 min to 10 min, 15 min, 20 min, 3 hour and 5 hour as the salt concentration is changed from 0.7 mM to 1.5 mM, 2 mM, 3 mM, 10 mM and 300 mM, respectively. Finally, the solution was centrifuged at 7,500 rpm for 7 min to eliminate any unreacted residues. After removing the supernatant, synthesized nanoparticles were redispersed in deionized water for further measurement.

Various sizes of Ag bodies on 40-nm DNA-modified Au head with a thin plasmonic neck were synthesized by controlling the amount of AgNO3. 2% PVP, 0.1 M L-SA, and 1 mM AgNO3 were controlled to contain the same molar ratio as 100 (PVP/Ag+) and 50 (L-SA/Ag+).

To form a 30 nm Ag body, 100 μL of 70 pM DNA-modified AuNP solution in phosphate-buffered saline (0.3 mM NaCl, 10 mM phosphate buffer) was reacted with 4.54 μL of 1 mM AgNO3 solution in the presence of 2.5 μL of 2% PVP and 2.3 μL of 0.1 M L-SA. For 55, 65 and 75-nm AgNPs, 100 μL of 70 pM DNA-modified AuNP solution was dispersed in 0.7 mM, 1 mM and 2 mM NaCl, respectively, containing 10 mM phosphate buffer and reacted with 32.6 μL, 59.8 μL and 87.9 μL of 1 mM AgNO3 solution, respectively, while maintaining the same molar ratio of PVP/Ag and L-SA/Ag. The resulting mixture was mildly pipetted for several minutes until solution color starts to change and kept in an orbital shaker at room temperature. Finally, the resulting solution were centrifuged at 10,000, 7,500, 6,000 and 5,500 rpm for Au-Ag head-body nanosnowman with ~ 30, 40, 65 and 75-nm Ag bodies, respectively, for 7 min to eliminate any unreacted residues. After removing the supernatant, the synthesized nanoparticles were redispersed in deionized water. For synthesizing Au-Ag snowmen with different sizes of Au head, 100 μL of 30 pM DNAmodified 50 or 60-nm AuNPs in 0.3 mM or 0.5 mM NaCl, respectively, containing 10 mM phosphate buffer was reacted with 13.4 μL and 20.5 μL of 1 mM AgNO3 solution in the presence of 7.45 μL and 11.4 μL of 2% PVP and 6.7 μL and 10.2 μL of 0.1 M L-SA, respectively, to form

50 and 60-nm Ag bodies, respectively. After removing the supernatant, the synthesized nanoparticles were redispersed in deionized water.

1.3. Results and Discussion

Au–Ag head–body nanosnowmen were synthesized using DNA–modified AuNPs (DNA–AuNPs) as seeds and adding Ag precursors and other reagents to deposit an AgNP on DNAAuNP surface (Figure 1). The key controlling reagent to control the junction morphology of the nanosnowman is salt (NaCl in this case).3 In a typical experiment, 40 nm AuNPs were modified with thiolated–DNA and centrifuged to remove the excess amount of DNA and salts. The resulting particles were then redispersed in 10 mM phosphate buffer (PB) with a desired NaCl concentration. In the DNA–AuNP solution, poly(vinylpyrrolidone) (PVP), (+)–sodium L–ascorbate (L–SA), and AgNO3 in deionized water were added sequentially for the asymmetric growth of AgNP on the surface of DNA–AuNP. The reaction kinetics for the asymmetric growth of AgNPs on DNA–modified AuNPs is strongly affected by salt concentration, and much faster reaction was observed at lower concentration. In the presence of NaCl, Ag+ usually forms AgCl precipitates, but Ag+ can be stabilized via the lone–pair electrons of O or N atoms of PVP.3,47 To precisely control the plasmonic neck morphology between Au head and Ag body particles, salt concentration was varied from high to very low concentrations while all the other conditions were kept same

(Figure 1A). The 3D finite element method (3D FEM) calculation results (COMSOL, Stockholm, Sweden) show that the electromagnetic field around the neck junction is largely enhanced while narrowing the neck region between Au head and Ag body (the electromagnetic field enhancement and distribution with 633 nm light source are shown in Figure 1A). The structural changes were confirmed with the transmission electron microscopic (TEM) images as shown in Figure 1. Please notice that Au head and Ag body sizes were fixed at ~40 and ~55 nm, respectively in Figure 1A. At a relatively high salt concentration (10 mM), very thick and indistinct neck junction between Au head and Ag body was formed (Figure 1A-1:,indistinct neck). When salt concentration was further lowered, a much faster reaction rate was observed, and, importantly, the junction area became narrower as salt concentration was lowered to 3 and 0.7 mM (Figures 1A-2, thick neck and Figure 1A-3, thin neck). When salt concentration was further decreased to <0.7 mM, a variety of nanostructures including core-satellite-type structures were formed in a rather uncontrollable fashion (Supporting Information Figure S1). The key factor for the asymmetric growth is the competition between precipitation and stabilization of AgCl.[3] This means the relative ratio between Ag precursor and salt amounts is critical in controlling the junction morphology between Au head and Ag body. We found that a relative molar ratio of the molar concentration of salt to the molar concentration of Ag precursor should be maintained between 1 and 3 to form the plasmonic nanosnowman structures with a very thin neck junction and high structural reproducibility. Next, we controlled the size of Ag body by tuning the added amount of silver precursors. The final salt concentrations were adjusted to be 0.3, 0.5, and 1 mM for 30, 40 and 65 nm Ag body sizes, respectively (see the Supporting Information for more details). Figure 1B–i, ii, and iii show the size of Ag body was well controlled from the size that is smaller than Au head (Figure 1B–i) to the size that is larger than Au head (Figure 1B–iii). In the case of Figure 1B–ii, the size of Au head matches well with the size of Ag body. For more reliable characterization of the AgNP size, more than 200 of particles were analyzed for each case with TEM images using ImageJ program (rsb.info.nih.gov/ij). The average sizes of Ag bodies were confirmed as 30, 40, 55, and 65 nm for Figure 1B–i, 1B–ii, 1A–3, and 1B–iii, respectively (size deviation was <10% for all cases). To understand the relationships between structural change in the Au–Ag head–body nanosnowmen and plasmonic signal response, the UV–vis extinction spectra were measured and correlated with TEM images. Figure 2 shows the normalized UV–vis spectra taken from a series of samples with different salt concentrations and different Ag body sizes. In Figure 2A, one can readily notice that the plasmon modes between 550 and 1100 nm are strongly affected by change in salt concentration. In the plasmonic dimers with a gap between particles, the low-frequency plasmon modes are resulted from the coupling between two dipole modes of each particle. [13,19,28,29,32,39] However, in the case of our merged Au-Ag head-body nanosnowman with a conductive overlap, the low-frequency plasmon mode corresponds to charge-transfer plasmon that is a true dipolar mode and is different from the dimers with a gap because this structure can have a net charge on each of Ag and Au particles through a conductive region.[13,28,39,40,48] In Figure 2A, the maximum peak of charge-transfer plasmon mode was red shifted from 617 to 970 nm by lowering the salt concentration for the nanosnowman with a 55 nm Ag body. In Figure 2A, the numbered spectra correspond to the structures in Figure 1A-1 (indistinct neck), 1A-2 (thick neck), and 1A-3 (thin neck), respectively, that show that decrease in the degree of overlap between Au head and Ag body as salt concentration decreased. Our experimental observations are matched well with reported theoretical and experimental results.[13,28,39,40,48] These results imply that charge-transfer plasmon mode is highly sensitive to structural change in the junction region of the nanosnowmen. Figure 2B shows the spectra for the nanosnowmen with differently sized Ag bodies on 40 nm Au head. As the size of the

Ag body increases, the charge−transfer mode was further red shifted from 687 to 825, 970, 992, and >1000 nm for 30, 40, 55, 65, and 75 nm Ag bodies, respectively. These red shifts were due to change in the aspect ratio and longitudinal plasmon energy.[48] The maximum intensity of this mode was decreased as the size of Ag body was increased. In general, the intensity of the resonance plasmon mode is determined from the effective charge separation with a mirror symmetry because this provides the main restoring force for electron oscillation.[3,49] One possible explanation for the decreased intensity is that the composition of the Au−Ag bimetallic nanosnowman primarily affects the anisotropy of the mirror symmetry and the larger size of Ag body makes the nanosnowman structure more asymmetric. Further, AgNPs scatter light more strongly than AuNPs, and these uneven scattering contributions from Au head and Ag body make the nanosnowman more asymmetric as the Ag body size increases. In contrast to the charge−transfer plasmon, plasmon modes at transverse region become more intense with larger Ag body size. This makes sense because the intensity of extinction is affected by the overall size of nanostructures and the mirror symmetry remains in the transverse direction for the strong restoring force of electron oscillation. As lowering the salt concentration to <3 mM, a new plasmon mode starts to appear between 550 and 700 nm in Figure 2A, and this mode becomes more clear when the plasmonic neck region between Au head and Ag body becomes sharper (Figures 2A and inset). The UV–vis spectra of Au–Ag nanosnowmen for indistinct (1), thick (2), and thin (3) necks were fitted with the five–parameter Lorentz function to extract this new plasmon mode (Figure 2C and Supporting Information Figure S3). The maximum wavelengths of the new plasmon modes were confirmed to be 595, 608, and 614 nm for indistinct, thick, and thin necks that correspond to 2, 1.5, and 0.7 mM NaCl, respectively. As the size of Ag body increases, this mode is more red shifted (Figure 2B). This mode corresponds to bonding dipole–dipole plasmon from the capacitive coupling of charges that pile up within the neck area between Au head and Ag body. This capacitive plasmon coupling has been recently proposed for touching and nearly touching nanospheres,[39] nanorods,[48] and nanocube dimers and observed by the near–field imaging of the induced electric field using the aperture–less near–field scanning optical microscopy (ANSOM).[50] However, the precise morphology control of the connecting area between two particles has not been achieved in the above studies. According to a theoretical calculation, the energy and intensity of this capacitive mode is highly sensitive and red shifted as a narrower junction structure is formed.[39,48,50] Our scheme is powerful in precisely and reproducibly controlling narrow plasmonic junction morphologies and is consistent with this theoretical result. Beside charge−transfer and capacitive plasmons in the longitudinal region, Figure 2 also shows various plasmon modes in the transverse region of Au−Ag nanosnowmen. Recent studies with plasmonic heterodimers have shown that there are unique couplings between various plasmon modes, which are the dark modes that were not found in plasmonic homodimers.[31−33,48] This is mainly due to the broken symmetry, induced from different compositions or sizes of monomeric components. For example, the antibonding mode, dark in symmetric dimers, becomes bright and excitable in asymmetric dimers due to the nonzero net dipole moment of the antibonding mode. Moreover, when nanoparticle size is large enough (>50 nm), the contribution of multipolar localized surface plasmons is increased.[32] As a result, diverse plasmon couplings between dipolar and multipolar localized surface plasmons in the asymmetric Au−Ag nanosnowman structures can be induced. This asymmetrically coupled additional excitation can contribute to bonding and antibonding plasmon modes and make spectral features complicated in asymmetric structures. By carefully considering the reported theoretical calculations and experimental results, three distinctive plasmon modes at the transverse region in Figure 2C can be assigned to antibonding dipole−quadrupole, antibonding dipole−dipole, bonding dipole−quadrupole, bonding dipole−dipole, and charge−transfer plasmon modes in order of decreasing energy. Via the diverse excited plasmon modes, Au−Ag nanosnowmen show the broad and tunable LSPR spectrum across the visible and near−infrared range, suggesting the usefulness of these probes with a variety of different excitation laser sources. These nanosnowman particles with a narrow conductive junction can generate strong SERS signals because these structures allow for forming the plasmonically enhanced EM field and positioning Raman−active molecule in a hot spot with strong EM field by DNA. Moreover, the LSPR spectrum of Au−Ag nanosnowman structures cover from the visible to nearinfrared range that is ideal for multiple laser wavelengths. We carried out Raman signal measurements from the Raman−dyelabeled nanosnowmen with three different excitation laser wavelengths (514, 633, and 785 nm laser wavelengths; the SERS signals in Figure 3 were obtained in solution with 10 mW laser power and 3 s acquisition time). We used FAM dye with the absorption maximum at 495 nm to minimize the resonance effect of a dye (please notice that the dyes were densely modified on Au head surface; Figure 1A), and SERS signals were detected with all three excitation wavelengths (Figure 3D and Supporting Information Figure S4). The characteristic peaks of FAM dye at 1180 and 1325 cm−1 were well matched with the reported spectra.[51,52] To explore how structural change in the nanosnowman affects SERS signal, Raman signals from the synthesized particles with different salt concentrations and varying Ag body sizes were correlated with the TEM images and 3D FEM calculation results (Figures 1 and 3C). Figure 3D shows the measured SERS spectra from the 40 nm Au head−55 nm Ag body nanosnowmen with varying plasmonic neck morphologies. For 300 mM salt concentration, spherical Ag shell was formed on DNA−AuNPs, and nearly no SERS signals were detected in this case (Figure 3A and Supporting Information Figure S5). In the case of 10 mM salt concentration (Au head−Ag body with an indistinct neck), the SERS signal became weakly detectable (Figure 3A−1,D−1). When salt concentration was decreased to 3 mM or lower, SERS signal became much stronger with distinctive spectral features as the neck region between Au head and Ag body became sharper (thick−neck case; Figure 3A−2,D−2). With very low salt concentration (0.7 mM), the neck region became very narrow and sharp, the strongest SERS signal was detected (thin−neck case; Figure 3A−3,D−3). Because the peak at 1325 cm^{-1} generated the highest signal−to−noise ratio, we used this peak as the standard peak. The SERS spectral peak intensity at 1325 cm^{-1} was plotted as a function of NaCl concentration with multiple excitation laser sources (514, 633, and 785 nm; Figure 3A). For 514 and 633 nm excitation sources, it is clear that the SERS signal gets stronger as the neck region becomes narrower and sharper (please also see Figure 3C for the EM field distributions). However, in the case of 785 nm excitation laser, the SERS signal got stronger at 3 mM salt concentration but did not get any stronger with lower salt concentrations mainly because of the mismatch between the SPR of the nanostructure and laser wavelength (Figures 2A and 3A). As stated before, the large EM field within the plasmonic neck region can be due to charge-transfer plasmon, capacitive plasmon and broken symmetry.[20,39,40,48] To study the relationships between plasmon mode, electromagnetic field distribution, and SERS response, 3D FEM calculation was used (Figure 3C). Our simulation results show the charge distributions of the nanosnowmen with a conductive junction at three different excitation wavelengths and how the plasmon mode of the nanosnowmen can act as a single dipole or multipole. [13,39,48,50,53,54] In particular, the nanosnowman structure with a narrow and sharp neck junction generated a stronger EM field with a highly localized field around the neck part while more delocalized EM field was observed from the nanosnowman structures with a thick and blunt neck. Interestingly, the reversed charge distributions for Au and Ag are observed at shorter wavelengths, and this is because less electronegative Ag needs higher energy to excite Ag body part to a negatively charged state. Our calculation results clearly show that large charge build−ups at the opposite sides of the plasmonic neck junction, and stronger EM field was induced as the neck junction becomes narrower and sharper (Figure 3C). Importantly, the charge transfer mode was red shifted as the conductive junction became narrower and sharper in both experimental and calculation results. In particular, a very strong charge−transfer mode was observed from a thin−neck nanosnowman with 1005 nm incident light (the bottom right image of Figure 3C), and this near−infrared light−induced strong EM field result at ~1000 nm matches well with the experimental result for the thin−neck snowman case (the red spectrum in Figure 2C). The broad spectrum around 1000 nm in Figure 2C can be attributed to small differences in the junction morphology for a large number of nanosnowman structures with a narrow neck, and even a little change in the junction morphology can affect the extinction maximum.[13,39,48,54] The overall trends for the experimental results from the UV−vis spectra and SERS signals match well with the calculated EM field results (Figures 2A and 3A,C). It should be noted that there is the resonance effect that could result in a stronger SERS signal in the case of 514 nm incident light because of the partial overlap between the wavelength of the incident light, the absorption spectrum of the dye and the LSPR spectrum of the nanosnowman with a thin neck, and the position of the dye and the distance between the dye and nanoparticle surface can also affect SERS signal intensity. Our results suggest that the narrow and sharp morphology of the plasmonic neck region is the key for obtaining large EM fields, the near−infrared signal, and strong SERS signals from the nanosnowman structures, and plasmon modes are largely affected and controlled by the junction morphology. The optical stability of this structure was maintained over three months at room temperature or >six months at 4 ° C. We then studied the correlations between the size of the Ag body and SERS intensity while varying excitation laser wavelengths (Figure 3B). Figure 3B shows changes in the distinctive spectral peak of FAM dye at 1325 cm−1 as a function of Ag body size with 40 nm Au head. Overall trend is that a stronger SERS signal was observed as the Ag body became larger, and 514 or 633 nm excitation source generated larger signals than 785 nm laser source. An interesting point here is that the SERS signal exponentially increased as the Ag body size became similar to or larger than the Au head size. This is mainly because a larger Ag particle will introduce size and structural anisotropicity and compositional heterogeneity−based larger EM field; several plasmon modes such as dipolar or multipolar modes can be hybridized to generate a strong plasmonic coupling due to a broken symmetry.[33]

Next, we tested the multiplexing capability of the Au-Ag nanosnowman probes with a variety of different Raman dyes. In particular, we investigated the resonance effect of Raman dyes with three different excitation laser wavelengths to show the tunability and applicability of these probes over the visible and near-infrared range. In a typical experiment, we used six different Raman dyes, Oregon Green (ORG), Cy3, Cy5, Alexa Fluor 546 (Alexa 546), Alex Fluor 647 (Alexa 647), and Alexa Fluor 750 (Alexa 750). For all six cases, the dyes were positioned close to AuNP surface [5′ -CAC GCG TTT CTC AAA-PEG18-A10-Raman Dye-(CH2)3-SH-3′]. These Raman dyes can cover visible to near-infrared range, and the absorption maxima of these Raman dyes are 498, 550, 648, 555, 650, and 753 nm for ORG, Cy3, Cy5, Alexa 546, Alexa 647, and Alexa 750, respectively. It is known that the resonance effect of SERS dyes can be maximized when the absorption maximum wavelength of dyes is close to or matches with that of excitation laser [surface-enhanced resonance Raman scattering (SERRS)].[55,56] The distinctive Raman spectra of all Raman dyes are shown in Supporting Information Figure S6, and the marked peaks were used as the fingerprint peaks for each case. The strongest SERS signals were observed when the absorption maximum of a dye is close to the wavelength of an excitation laser (Figure 4). It should be noticed that 100 pM nanoparticle concentration was used for the nonresonance conditions, and the SERRS spectra at an excitation laser wavelength that is close to that of absorption maximum of each Raman dye were taken from a lower concentration of nanoparticles (20, 20, 5, 33, 5, and 5 pM for ORG, Cy3, Cy5, Alexa 546, Alexa 647, and Alexa 750) and rescaled for comparison. The laser resonance effects for each dye generated 4 and 35-fold higher SERS signal intensity at 514 nm wavelength than 633 and 785 nm excitation wavelengths for ORG, 7 and 60-fold higher signal intensity with 514 nm laser than 633 and 785 nm excitation wavelengths for Cy3, 64 and 14-fold higher signal at 633 nm wavelength than 514 and 785 nm excitation wavelengths for Cy5, 17 and 118- fold higher signal at 514 nm than 633 and 785 nm excitation wavelengths for Alexa 546, 143 and 18-fold higher signal intensity at 633 nm than 514 and 785 nm excitation wavelengths for Alexa 647, and 161 and 14-fold higher signal intensity at 785 nm than 514 and 633 nm excitation wavelengths for Alexa 750, respectively. The resonance effects from Raman dyes with different absorption maxima were confirmed to be enhanced by ~ one to two orders of magnitude when the dyes were excited at a resonance wavelength, and these values are comparable to the reported results.[51,55] The strong SERRS can be achieved when an excitation laser wavelength is close to the LSPR maximum of plasmonic structures and the electronic resonance frequency of molecules such as fluorophore.[51,55–57] It should be also noted that most studies on the SERRS effect have been based on aggregated spherical nanoparticles via salt or periodic arrays to generate plasmonic gap structures with hot spots. In these strategies, however, it is difficult to control the number of particles in an aggregate and the distance between particles within an array, which are the critical factors for the intense EM field and the tunability of LSPR signal. Considering these aspects, the DNA-functionalized Au–Ag head–body nanosnowman with a highly controllable plasmonic neck junction are suitable as multiplexable SERRS probes. We also tested how quantitatively and reproducibly one can get signals from the nanosnowmen in the next sets of experiments. First, the SERS intensity as a function of particle concentration was plotted with the thin neck structures (Figure 1A-3). For the nonresonant cases, the SERS intensity at 1325 cm^{-1} from FAM dyes was plotted as a function of nanoparticle correlations with relatively small standard deviations. These results can be attributed to the positional uniformity of Raman dyes and the structural uniformity, especially in the junction area, of the snowman nanoparticles. The lowest detectable particle concentration was confirmed to be 1 pM with the nonresonant FAM Raman dyes. Next, Cy5 dyes with the absorption maximum at 648 nm was used as the resonant dyes. For the resonance condition with 633 nm excitation laser, the lowest detectable particle concentration was 5 fM, which represents two orders-of-magnitude improvement in detection limit (Figure 5B). Over 1-100 fM range, the signal intensity increased linearly with clearly discernible difference in signal intensity for different concentrations. Finally, the SERS enhancement factors (EFs) without the resonance effect of dyes were calculated from the Au-Ag head-body nanosnowmen in Figure 1A-3. The SERS spectra were measured with dried samples that had been spin-coated on a silicon wafer (see the Supporting Information for the experimental details and calculations). The loading number of dyes per particle was determined based on fluorescence measurements. The calculated enhancement factors were 1.6 ± 0.4 × 106 with a range of 1.3 × 106 to 1.9 × 106. It should be noted that although the strong SERS effect can be obtained within the plasmonic neck region the calculated enhancement factors in this case are from all the modified dyes on the whole snowman particle surface. For this reason, our EF calculation does not represent the plasmonic enhancement within the neck crevice region.[39,40,48] In addition, when the resonance effect is considered, the EF value is $>10^8$. It is now widely accepted that 10^6-10^8 EF values could be large enough even for singlemolecule detection,[1,2,16,19,20] and more important issues are the uniformity of nanostructures and the reproducibility of SERS signals. Considering the structural uniformity and excellent controllability of the plasmonic junction over a large number of particles, the nanosnowmen with a conductive junction can be the promising SERS probes with high sensitivity and reliability.

1.4. Conclusions

In summary, we showed that the plasmonic conductive junction of Au–Ag head–body nanosnowman particles can be highly tunable with salt–controlled chemistry for the anisotropic Ag structure growth on thiolated DNA–modified AuNPs. These finely controllable structures with a high synthetic yield (~95%) have a conductive neck junction with charge–transfer and capacitive plasmon modes and the compositional and structural asymmetry. By introducing a budding Ag body structure on an Au head, plasmon modes including charge transfer and capacitive modes can be excited in a controllable fashion and reflected on the optical spectra. Via the fine controlling of the conductive junction, a variety of different EM fields were generated within the nanosnowman structures mainly due to different plasmon couplings and broken symmetry, and the strongest EM field was observed in the crevice area around the thin conductive junction of the snowman. Our FEM–based calculation results show that the narrow and sharp morphology of the plasmonic neck region is the important features to generate large EM fields and strong SERS signals, and the plasmon modes from the nanosnowman structures are largely governed by the junction morphology. It was experimentally and theoretically shown that the extinction peak for the charge transfer plasmon mode can be tuned by controlling the conductive junction of the nanosnowman structure, and very strong near-infrared light-induced EM field was observed from the nanosnowman structure with a narrow and sharp neck morphology. We have also shown that quantitative and reproducible SERS signals can be generated from the Au-Ag head-body nanosnowmen with a nonresonant Raman dye at 514, 633, and 785 nm excitation laser sources, and by selecting a proper resonant Raman dye with an absorption maximum that is close to the excitation wavelength the signals from probes were further enhanced and the signals from 5 fM nanosnowman solution were clearly detectable. With the resonance effect, >108 EF values can be obtained from the Au-Ag head-body nanosnowman structures with a very thin neck junction and sharp crevices around the junction. Our strategy in designing and synthesizing plasmonic nanosnowman structures with the highly precise synthesis of the thin conductive junction and high yield synthesis of the targeted snowman structures opens revenues in studying and utilizing plasmonic nanostructures with strong, controllable, and quantifiable plasmonic signals, and the results shown here provide new insights and data for plasmonic nanostructures with a conductive junction. Finally, the plasmonic nanosnowman structures can be readily used for various applications including SERS-based chemical and biological sensing, nanoantenna and solar cell.

1.5. References

1. Lim, D.–K.; Jeon, K.–S.; Kim, H. M.; Nam, J.–M.; Suh, Y. D. *Nat. Mater.* 2010, **9**, 60–67.

2. Lee, J.–H.; Nam, J.–M.; Jeon, K.–S.; Lim, D.–K.; Kim, H.; Kwon, S.; Lee, H.; Suh, Y. D. *ACS Nano* 2012, **6**, 9574–9584.

3. Lee, J.–H.; Kim, G.–H.; Nam, J.–M. *J. Am. Chem. Soc.* 2012, **134**, 5456–5459.

4. Lim, D.–K.; Jeon, K.–S.; Hwang, J.–H.; Kim, H.; Kwon, S.; Suh, Y. D.; Nam, J.–M. *Nat. Nanotechnol.* 2011, **6**, 452–460.

5. Prodan, E.; Radloff, C.; Halas, N. J.; Nordlander, P. *Science* 2003, **302**, 419–422.

6. Liu, G. L.; Yin, Y.; Kunchakarra, S.; Mukherjee, B.; Gerion, D.; Jett, S. D.; Bear, D. G.; Gray, J. W.; Alivisatos, A. P.; Lee, L. P.; Chen, F. F. *Nat. Nanotechnol.* 2006, **1**, 47–52.

7. Chu, M.–W.; Myroshnychenko, V.; Chen, C. H.; Deng, J.–P.; Mou, C.–Y.; García de Abajo, F. J. *Nano Lett.* 2008, **9**, 399–404.

8. Mulvihill, M. J.; Ling, X. Y.; Henzie, J.; Yang, P. *J. Am. Chem. Soc.* 2009, **132**, 268–274.

9. Lee, H.; Lee, J.–H.; Jin, S. M.; Suh, Y. D.; Nam, J.–M. *Nano Lett.* 2013, **13**, 6113–6121.

10. Lee, H. M.; Lee, J.–H.; Kim, H. M.; Jin, S. M.; Park, H. S.; Nam,

J.–M.; Suh, Y. D. *Phys. Chem. Chem. Phys.* 2013, **15**, 4243–4249.

11. Lee, J.–H.; Hwang, J.–H.; Nam, J.–M. *Wiley Interdiscip. Rev.: Nanomed. Nanobiotechnol.* 2013, **5**, 96–109.

12. Fan, J. A.; Wu, C.; Bao, K.; Bao, J.; Bardhan, R.; Halas, N. J.; Manoharan, V. N.; Nordlander, P.; Shvets, G.; Capasso, F. *Science* 2010, **328**, 1135–1138.

13. Lassiter, J. B.; Aizpurua, J.; Hernandez, L. I.; Brandl, D. W.; Romero, I.; Lal, S.; Hafner, J. H.; Nordlander, P.; Halas, N. J. *Nano Lett.* 2008, **8**, 1212–1218.

14. Xu, H.; Bjerneld, E. J.; Ka¨ll, M.; Bo¨rjesson, L. *Phys. Rev. Lett.* 1999, **83**, 4357–4360.

15. Nie, S.; Emory, S. R. *Science* 1997, **275**, 1102–1106.

16. Etchegoin, P. G.; Le Ru, E. C. *Phys. Chem. Chem. Phys.* 2008, **10**, 6079–6089.

17. Moskovits, M. *J. Raman Spectrosc.* 2005, **36**, 485–496.

18. Kneipp, K.; Wang, Y.; Kneipp, H.; Perelman, L. T.; Itzkan, I.; Dasari, R. R.; Feld, M. S. *Phys. Rev. Lett.* 1997, **78**, 1667–1670.

19. Willets, K. A.; Van Duyne, R. P. *Annu. Rev. Phys. Chem.* 2007, **58**, 267–297.

20. Wustholz, K. L.; Henry, A.–I.; McMahon, J. M.; Freeman, R. G.; Valley, N.; Piotti, M. E.; Natan, M. J.; Schatz, G. C.; Duyne, R. P. V. *J. Am. Chem. Soc.* 2010, **132**, 10903–10910.

21. Pazos−Perez, N.; Wagner, C. S.; Romo−Herrera, J. M.; Liz−Marzan, L. M.; García de Abajo, F. J.; Wittemann, A.; Fery, A.; Alvarez−Puebla, R. A. *Angew. Chem., Int. Ed.* 2012, **51**, 12688−12693.

22. Xu, H.; Aizpurua, J.; Ka¨ll, M.; Apell, P. *Phys. Rev. E* 2000, **62**, 4318−4324.

23. Chuntonov, L.; Haran, G. *Nano Lett.* 2011, **11**, 2440−2445.

24. Yan, B.; Boriskina, S. V.; Reinhard, B. r. M. *J. Phys. Chem. C* 2011, **115**, 4578−4583.

25. Nehl, C. L.; Liao, H.; Hafner, J. H. *Nano Lett.* 2006, **6**, 683−688.

26. Kooij, E. S.; Ahmed, W.; Zandvliet, H. J. W.; Poelsema, B. *J. Phys. Chem. C* 2011, **115**, 10321−10332.

27. Wei, H.; Zhang, S.; Tian, X.; Xu, H. Proc. *Natl. Acad. Sci. U.S.A.* 2013, **110**, 4494−4499.

28. Savage, K. J.; Hawkeye, M. M.; Esteban, R.; Borisov, A. G.; Aizpurua, J.; Baumberg, J. J. *Nature* 2012, **491**, 574−577.

29. Esteban, R.; Borisov, A. G.; Nordlander, P.; Aizpurua, J. *Nat. Commun.* 2012, **3**, 825.

30. Kulkarni, V.; Prodan, E.; Nordlander, P. *Nano Lett.* 2013, **13**, 5873−5879.

31. Fang, Z.; Cai, J.; Yan, Z.; Nordlander, P.; Halas, N. J.; Zhu, X. *Nano Lett.* 2011, **11**, 4475−4479.

32. Sheikholeslami, S.; Jun, Y.-w.; Jain, P. K.; Alivisatos, A. P. *Nano Lett.* 2010, **10**, 2655–2660.

33. Wang, H.; Wu, Y.; Lassiter, B.; Nehl, C. L.; Hafner, J. H.; Nordlander, P.; Halas, N. *J. Proc. Natl. Acad. Sci. U.S.A.* 2006, **103**, 10856–10860.

34. Taylor, R. W.; Lee, T.-C.; Scherman, O. A.; Esteban, R.; Aizpurua, J.; Huang, F. M.; Baumberg, J. J.; Mahajan, S. *ACS Nano* 2011, **5**, 3878–3887.

35. Larmour, I. A.; Faulds, K.; Graham, D. *J. Phys. Chem. C* 2010, **114**, 13249–13254.

36. Chen, G.; Wang, Y.; Yang, M.; Xu, J.; Goh, S. J.; Pan, M.; Chen, H. *J. Am. Chem. Soc.* 2010, **132**, 3644–3645.

37. Li, W.; Camargo, P. H. C.; Lu, X.; Xia, Y. *Nano Lett.* 2008, **9**, 485–490.

38. Novak, J. P.; Feldheim, D. L. *J. Am. Chem. Soc.* 2000, **122,** 3979–3980.

39. Romero, I.; Aizpurua, J.; Bryant, G. W.; García De Abajo, F. J. *Opt. Express* 2006, **14**, 9988–9999.

40. Atay, T.; Song, J.-H.; Nurmikko, A. V. *Nano Lett.* 2004, **4**, 1627–1631.

41. Shi, W.; Zeng, H.; Sahoo, Y.; Ohulchanskyy, T. Y.; Ding, Y.; Wang, Z. L.; Swihart, M.; Prasad, P. N. *Nano Lett.* 2006, **6**, 875–881.

42. Cozzoli, P. D.; Pellegrino, T.; Manna, L. *Chem. Soc. Rev.* 2006, **35**, 1195–1208.

43. Mokari, T.; Rothenberg, E.; Popov, I.; Costi, R.; Banin, U. *Science* 2004, **304**, 1787–1790.

44. Seo, D.; Yoo, C. I.; Jung, J.; Song, H. *J. Am. Chem. Soc.* 2008, **130**, 2940–2941.

45. Gu, H.; Yang, Z.; Gao, J.; Chang, C. K.; Xu, B. *J. Am. Chem. Soc.* 2004, **127**, 34–35.

46. Gu, H.; Zheng, R.; Zhang, X.; Xu, B. *J. Am. Chem. Soc.* 2004, **126**, 5664–5665.

47. Zhang, Z.; Zhao, B.; Hu, L. *J. Solid State Chem.* 1996, **121**, 105–110.

48. Slaughter, L. S.; Wu, Y.; Willingham, B. A.; Nordlander, P.; Link, S. *ACS Nano* 2010, **4**, 4657–4666.

49. Tan, S. J.; Campolongo, M. J.; Luo, D.; Cheng, W. *Nat. Nanotechnol.* 2011, **6**, 268–276.

50. Kim, D.–S.; Heo, J.; Ahn, S.–H.; Han, S. W.; Yun, W. S.; Kim, Z. H. *Nano Lett.* 2009, **9**, 3619–3625.

51. Stokes, R. J.; Macaskill, A.; Lundahl, P. J.; Smith, W. E.; Faulds, K.; Graham, D. *Small* 2007, **3**, 1593–1601.

52. Faulds, K.; McKenzie, F.; Smith, W. E.; Graham, D. *Angew. Chem., Int. Ed.* 2007, **46**, 1829–1831.

53. Scholl, J. A.; Garcia−Etxarri, A.; Koh, A. L.; Dionne, J. A. *Nano Lett.* 2013, **13**, 564−569.

54. Chen, F.; Alemu, N.; Johnston, R. L. *AIP Adv.* 2011, **1**, 032134.

55. Zhao, J.; Dieringer, J. A.; Zhang, X.; Schatz, G. C.; Van Duyne, R. P*. J. Phys. Chem. C* 2008, **112**, 19302−19310.

56. Itoh, T.; Yoshida, K.; Biju, V.; Kikkawa, Y.; Ishikawa, M.; Ozaki, Y. *Phys. Rev. B* 2007, **76**, 085405.

57. Yoshida, K.−i.; Itoh, T.; Biju, V.; Ishikawa, M.; Ozaki, Y. *Phys. Rev. B* 2009, **79**, 085419.

Figures

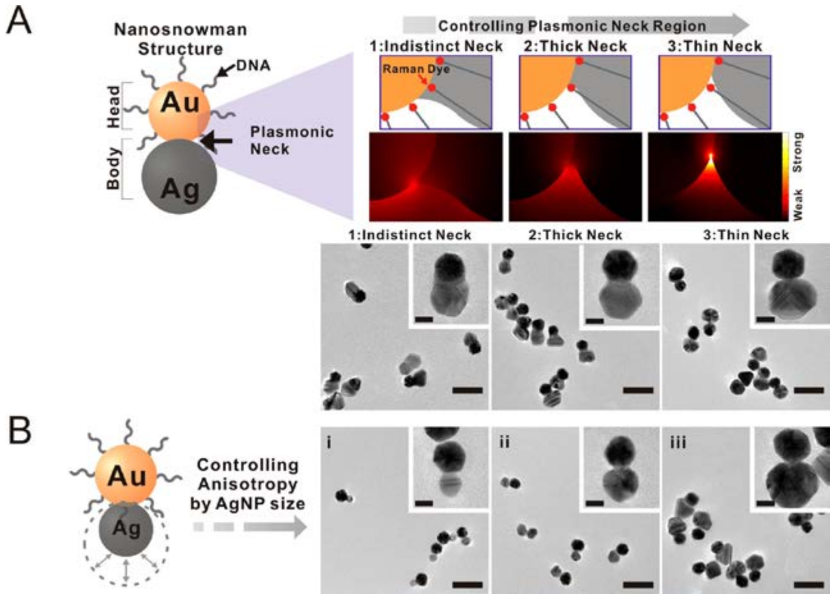

Figure 1. (A) Schematic, calculated electromagnetic field views and transmission electron microscope images of various Au–Ag head–body nanosnowman structures with various neck junction morphologies. Panels 1–3 for 40 nm Au–55 nm Ag head–body nanosnowmen at 10 mM, 3 mM and 0.7 mM salt concentrations, respectively. (B) Schematic and TEM images of Au–Ag head–body nanosnowman structures with different Ag body sizes. Panels i–iii for the snowmen with 40 nm Au head and 30, 40, and 65 nm Ag bodies, respectively. All the scale bars are 100 nm in the TEM images (the scale bars in the inset images are 20 nm).

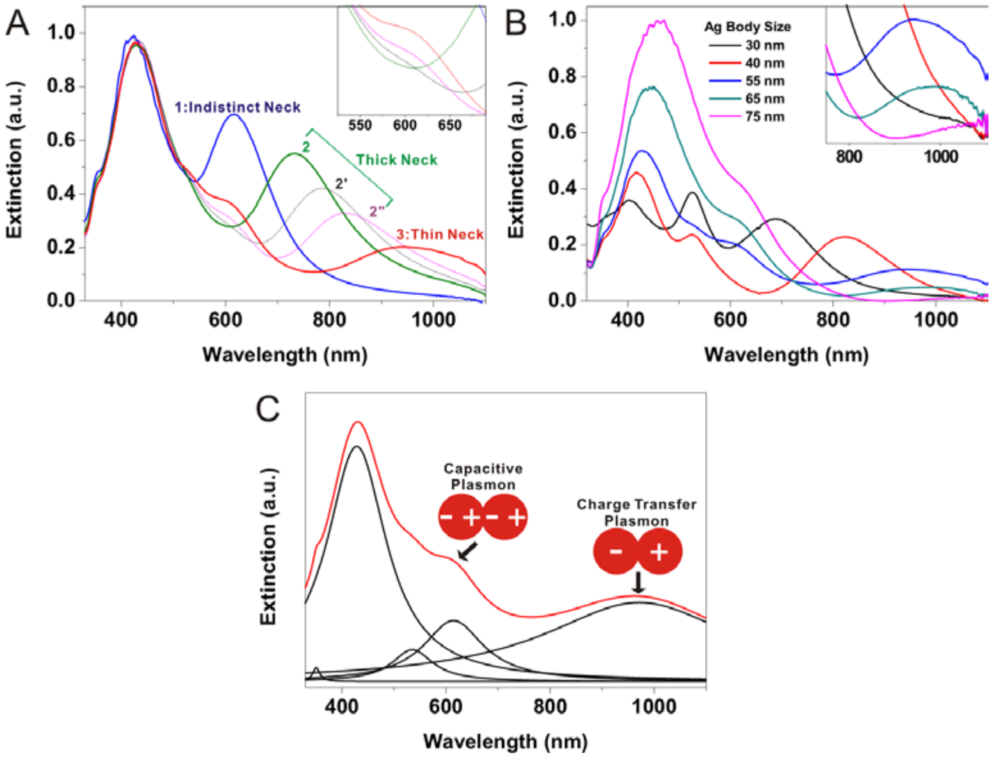

Figure 2. (A) The UV−vis extinction spectra of the Au−Ag head−body nanosnowmen with 40 nm Au head and 55 nm Ag body that correspond to the structural changes at different salt concentrations −10 mM NaCl (1, indistinct neck), 3, 2, and 1.5 mM NaCl (2, 2′ and 2″, thick neck), and 0.7 mM NaCl (3, thin neck). (B) The extinction spectra of Au−Ag head−body nanosnowmen with 40 nm Au head and different Ag body sizes. (C) The deconvoluted extinction spectra from Figure 2A (0.7 mM NaCl − 3, thin neck) with five−parameter Lorentz fitting.

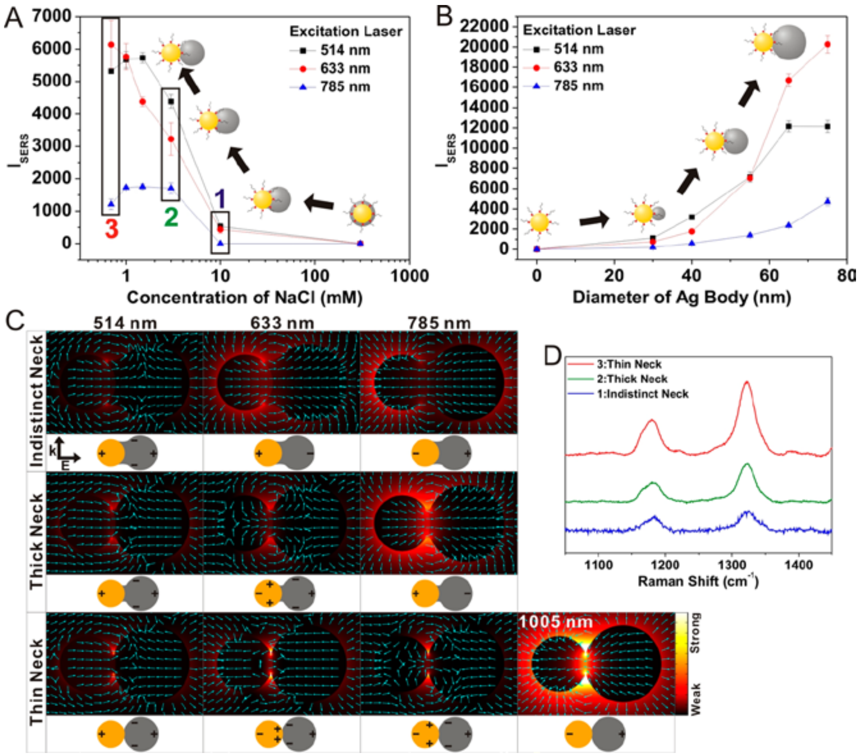

Figure 3. The change in electromagnetic field and SERS signal of nanosnowman structures. Conductive neck junction morphology−based change (A) and Ag body size−based change (B) in the SERS signal intensity at 1325 cm−1 with varying excitation laser wavelengths. (C) The 3D FEM calculation−based electromagnetic field enhancements and distributions with different plasmonic neck morphologies at 514, 633, 785, and 1005 nm excitation wavelengths. (D) SERS spectra of FAM dyes on head−body nanosnowmen from 10 mM NaCl (indistinct neck), 3 mM NaCl (thick neck), and 0.7 mM NaCl (thin neck) concentrations at 633 nm excitation wavelength.

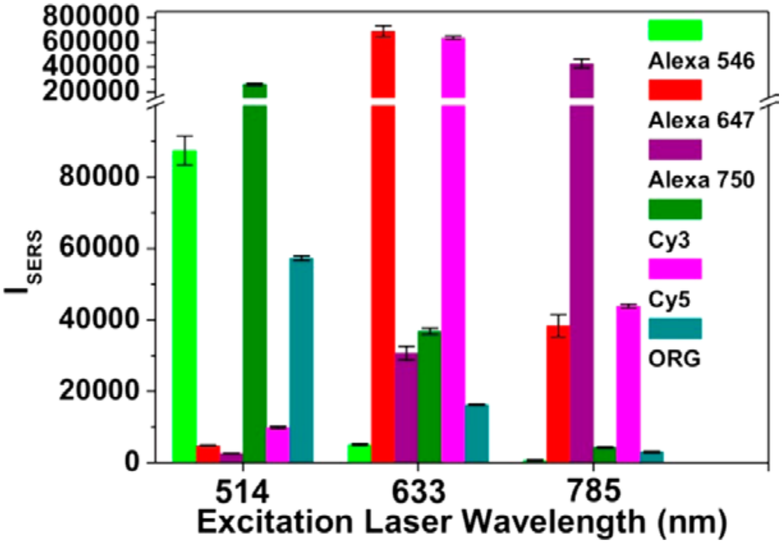

Figure 4. Comparison in the SERS intensities between different Raman dyes with the nanosnowman structure with a thin neck junction (structure 3) at 514, 633, and 785 nm laser wavelengths. All the spectra were taken with ~10 mW laser power, 10 s acquisition time, 20× objective lens, and static mode.

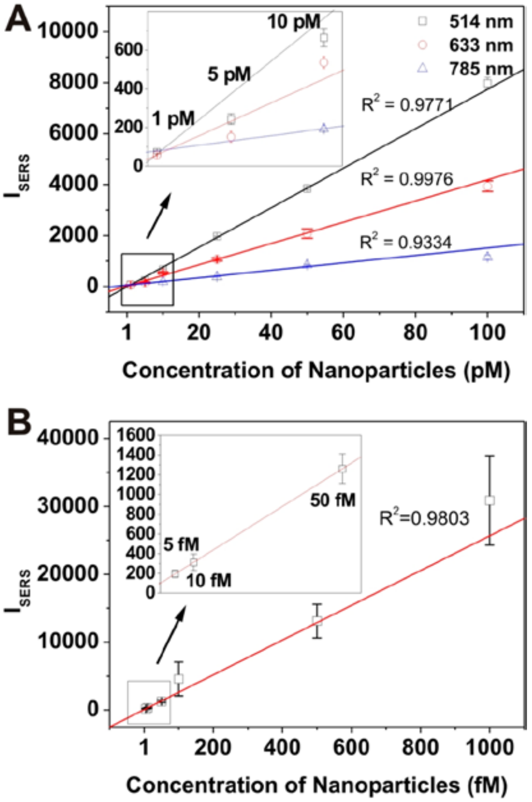

Figure 5. Nanosnowman concentration-dependent change in SERS intensity. (A) SERS intensity plot at 1325 cm−1 of FAM dye from Au-Ag head-body nanosnowmen in Figure 1A-3 as a function of nanoparticle concentration at three different excitation laser wavelengths (~10 mW laser power, 3 s acquisition time, and 20× objective lens.) (B) SERRS intensity plot at 1195 cm−1 of Cy5 Raman dye from same particles as a function of particle concentration at 633 nm excitation laser wavelength (~10 mW laser power, 10 s acquisition time, and 20× objective lens).

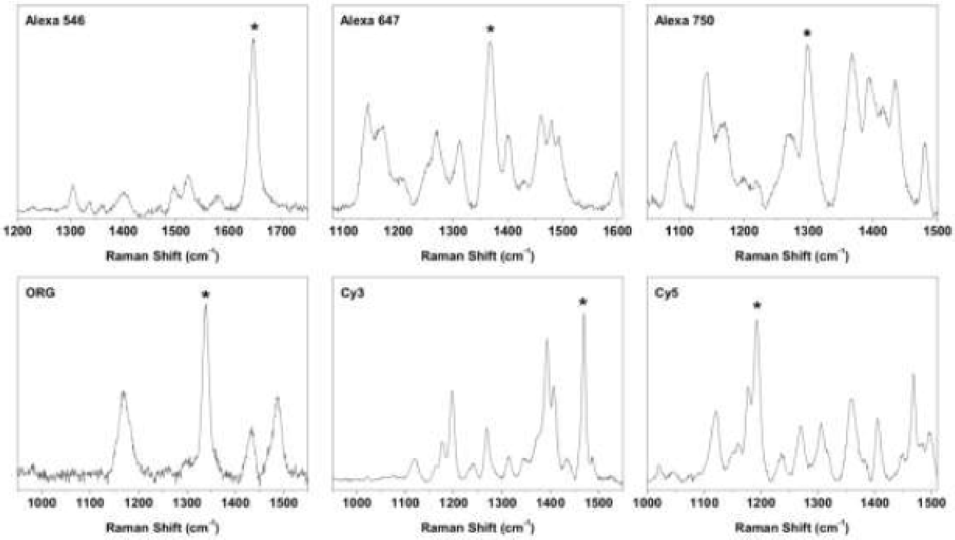

Figure 6. The representative surface-enhanced resonance Raman scattering (SERRS) spectra of ORG, Cy3, Cy5, Alexa 546, Alexa 647 and Alexa 750 Raman dyes on the nanosnowmen with 40-nm AuNP head and 55-nm AgNP body at the resonance excitation laser wavelengths.

Chapter 2

Kinetically Controlled Structures and Stacking Faults of Silver Body in Au(cube)–Ag Head–Body Nanostructures with Conductive Junction and Its Optical Properties

2.1. Introduction

With the tremendous development in nanotechnology, the fascinating properties of noble metal nanoparticles with localized surface plasmons (LSPs)[1-6], which represent the collective oscillations of conductive electrons induced by an external field, have been intensively studied in various fields due to their distinct optical properties depending on the size, shape, and composition of particles and dielectric environments.[2,4,5,8,13] To date, thanks to the efforts of many researchers, numerous single- and multicomponent nanostructures have been successfully synthesized using the bottom-up method.[5-8] Compared with the lithography-based top-down method, the bottom-up method allows more effective synthesis and control of nanostructures and can be extended to the synthesis of connected dimers or multimers. Although considerable research has been conducted on the synthesis of dimers, the precise control of the width and length of the conductive junction in the 10–20 nm range remains an important challenge in the bottom-up approach. The geometry-dependent conductive junction is a crucial factor for various optical properties, such as appearance and intensity of bonding dipolar plasmon (BDP)[18-25] or charge transfer plasmon (CTP) modes[26-32]. Hence, herein we propose the stacking-fault mediated 2nd body control in heterodimer structures which has controllable conductive junction of length and thickness as 10 to 20 nm regime. However, to date, the systematic engineering of stacking faults in colloidal nanoparticles has been rarely reported, especially in secondary metals grown on seed nanoparticles. Recently, Mirkin's group reported the stepwise evolution of multi-twinned secondary nanostructures developed over single-crystalline seeds under certain reaction conditions of plasmon-mediated synthesis[8]. Further, Chen's group demonstrated that the metal growth sites on Au seeds can be restricted by controlling the density of the ligand to induce crystal defects in the secondary silver nanostructures, thus generating hybrid structures such as Au spheres-Ag wires-Ag plates[40]. However, none of the previous reports touched upon the systematic engineering of stacking faults for the growth of certain anisotropic secondary structures on seeds together with their junction geometries. In multimetallic systems, the growth mode of secondary metals on seed nanoparticles is isotropic or anisotropic and is mostly governed by lattice mismatch[13-21], which impacts the growth modes as layered growth (Frank-van der Merwe (FM)) modes over 5% mismatch and island modes (Volmer–Webber (VW)). However, these general concepts are not applicable to the synthesis of asymmetric hetero Au/Au and Au/Ag nanostructures due to their indistinct lattice constant, which can generate a new plasmon mode or Fano–like outstanding optical properties[31–35]. Therefore, kinetics–controlling factors such as surface capping agent, reducing power of reductant, and supply of metal precursors become key factors to engineer the anisotropic growth of secondary metals in these compositions[9,11,17.] Therefore, our proposed method for stacking–fault mediated junction control in heterodimer structures is based on the delicate control of these kinetics parameters. Conductive junctions between two nanoparticles are crucial to study the optical properties of various plasmon modes. It is well known that when two nanoparticles are in close proximity to one another, strongly localized charges at the junction lead to considerably enhanced near–field distribution with the appearance of the bonding dipolar plasmon (BDP) mode[20–23]. In addition, when a conductive path is formed between two nanoparticles, oscillating electrical current across the junction allows the generation of CTPs[28–31,] and these plasmons strongly modify the optical spectrum and local–field distribution depending on the geometry and conductive properties of the junction. As reported by Halas and coworkers, it can be used as a nonperturbative monitor for optical frequency conductance[32−36] in a nanoscale junction; therefore, CTPs have recently attracted considerable research attention.

In this study, we control the structure of secondary metals and conductance of the evolved junction by delicate control of the kinetics parameters. By modifying the surface capping ligand on the seeds, a strong interaction was achieved between the ligand and seed nucleation sites accompanying the crystal defects in the secondary metal. Based on the crystal defects, we could control the secondary structures to be plate, truncated right bipyramid, and defect−rich bar structures. Also, by the delicate control of the kinetics parameters, we could control both conductance and peripheral junction geometry by tuning the secondary silver structures. The reaction conditions achieved the synthesis of a truncated right bipyramid junction with a width of ~20 nm and a length of ~1.5 nm, forming a 1 nm gap region between Au and Ag. On the other hand, a junction with a sub−10−nm width and ~10 nm length was developed using the silver bar structures. Thus, we found that small changes in the junction greatly affected the junction conductance and thus its optical properties, which determined the development of BPD and CTP modes. Interestingly, GC−SB did not generate both modes from the beginning of Ag growth, even though the conductance of the junction was not extremely low, as reported in previous studies. Our study of this precise control of stacking faults in the silver body, which enables the control of junctions (with dimensions in the 10–20 nm range) in heterodimer structures to achieve conductance−dependent optical properties, can be extended to various fields.

2.2. Experimental Section

2.2.1. Materials

All the chemical reagents [AgNO3, polyvinylpyrrolidone (MW 10,000 and 40,000), (+)−sodium ascorbic acid] were purchased from the Sigma−Aldrich (St. Louis, MO, USA) and used without further purification. Au nanocubes (GC) were synthesized by following previous reported protocols. HPLC−purified oligonucleotides and NAP−5 column were purchased from IDT, Inc.(Coralville, IA, USA) and GE Healthcare (Sephadex G−25 medium, DNA grade), respectively. NANO pure water (>18.0 MΩ, Milli−Q) was used for all the experiments. The formvar/carboncoated copper grid (Ted Pella, Inc. Redding, CA, USA) and TEM (JEM−2100, JEOL, Japan, 200 kV, from National Center for Inter−University Research Facilities at Seoul National University) were used for the TEM analysis.

2.2.2. Methods

Preparation of DNA−modified GCs. The modification of DNA on goldnanocubes was based on literature procedures.1−4 Oligonucleotides were reduced by dithiothreitol (DTT, 0.1 M) in phosphate−buffered saline solution (0.17 M, pH = 8.0) and then purified using a desalting NAP-5 column. For the preparation of DNA-modified AuNPs, purified DNA [5'-CACGCGTTTCTCAAA-(PEG)6-A10-(Cy3)-(CH2)3-SH-3'] were used to conjugate on AuNPs. The loading number of DNA was determined based on the fluorescence analysis. DNA modified AuNPs were mixed with 0.1M KCN for 10 min. The loading numbers of DNA per particle was determined to be 1,500 strands for 50 nm GCs. The excess amount of DNA (80 fold Cy3 dye) were added for DNA modification process. The solution was placed on a 60 ˚C oven for 30 min. Next, the resulting solution was adjusted to 0.3 M $NaNO_3$ (0.05 M × 2 and 0.1 M × 2) by the addition of salting buffer (2 M NaCl in 10 mM PB) every 20 min and heated for 5 min in a water bath at 90 ºC after each step to minimize the interactions between DNA bases and gold surface. After the salt-aging process, the solution was incubated overnight in a 60 ˚C oven. The solution was then centrifuged at 6,000 rpm for 10 min and the supernatant was removed carefully to get rid of unmodified DNA and unreacted reagents. The precipitate was redispersed in 10 mM PB solution (pH 7.4; this procedure was repeated two times). The concentration of DNAmodified GCs was characterized using the UV-Vis spectrophotometer (Agilent 8453 spectrophotometer, USA).

2.3. Result and Discussion

Figure 1a presents a novel scheme for synthesizing various Goldcube-head Silver-body (GC-S;body) hetero nanostructures. Our method can systematically engineer the silver body structures which contain stacking faults in Ag by controlling the reaction parameters. In the typical synthesis of GC-S;body hetero-nanostructures, seed-mediated growth was performed by preparing DNA-modified gold nanocubes (DNA-GC) as the seed according to previously reported methods with minor modifications. The resulting DNA-GC seeds were dispersed in 10 mM phosphate buffer (PB) and controlled amounts of poly(vinylpyrrolidone) (PVP), ascorbic acid (AA), and $AgNO_3$ were sequentially added for synthesizing various anisotropic silver-body structures such as plates (GC-SPs), truncated right bipyramids (GC-STRBs), and bars (GC-SBs) (Figure 1a). Notably, all the above mentioned parameters greatly affected the reaction kinetics and were important for determining the final structures. Among various kinetic parameters, DNA is a critical factor in forming anisotropic silver structures and has both physical and chemical functions. First, it acts as a physical barrier to restrict Ag growth at limited site of DNA-NC, shifting the growth mechanism from the FM mode (layered growth) to the VW mode (island growth) compared to that of bare GC. With the island growth mode, the total energy of the growing silver nuclei at the restricted sites increases, resulting in formation of crystal defects on the silver body. It increases particle anisotropy by impacting to the final morphologies of silver body due to the increased degree of symmetry breaking and can offer various features and functions. Second, the negatively charged phosphate backbone of DNA can chemically affect the reaction kinetics by accelerating the supply of Ag^+−PVP complexes which can also induce the atomic dislocation in silver body. Notably, stacking faults such as atomic dislocations or partially deposited atomic layers are energetically unstable site, resulting in preferential atomic deposition along it and generates anisotropic structures. The standard conditions were 50 μL of 10 pM GC seeds, 10 μL of 5% PVP, 25 μL of 0.1 M AA, and 75 μL of 0.08 mM $AgNO_3$. At this relatively high concentration of reducing agent and surfactant, silver plates (SPs) were formed at the vertex of GC with a yield of ~70%. The reaction was completed in ~5 s with an excess amount of AA as 250 ([AA]/[Ag+], 250) leads distribution of the degree of truncation and sizes, generating a mixture of triangular and hexagonal structures in the silver nanoplates. Further characterization of the GC−SP was performed using high−resolution transmission electron microscopy (HR−TEM) and selected area electron diffraction (SAED) analysis.

Similar to previous research, stacking faults or twin plane like crystal defects were observed on the silver body of the GC−SP. When the (111) plane of the silver plate in the GC−SP was parallel to the substrate, the diffraction pattern showed 1/3{422} reflections, which are typically forbidden in face−centered cubic (fcc) crystals. And HR−TEM image of vertically standing GC−SP on substrate, confirms an existence of stacking faults along the {111} planes. Interestingly, GC−STRBs were synthesized with a considerably improved yield (~90%) by adding an extremely low concentration of exceptional NaCl salt as 5 μM at the same reaction condition of GC−SP. Notably, the reduction rate of the silver precursor was strongly affected by NaCl addition, which caused a delay in the silver supply by forming AgCl precipitates or AgCl−PVP complexes. As previously reported, controlling the salt concentration could tune the plasmonic conductive junction as indistinct to sharp in Au−Ag bimetallic nanosnowman structures. In contrast to previous report, in our experiment, adding extremely small amount of NaCl could direct the structural transformation of Ag body from a plate to a truncated right bipyramid structures. Generally, nanoplates preferentially grow along the lateral direction due to the preferential deposition of newly generated atoms in energetically unstable crystal defect site. However, in our synthetic condition, the growth direction can be converted from lateral to vertical direction due to the NaCl, resulting in the formation of GC-STRBs instead of GC-SPs which of both share the same crystalline structures. The structural transformation of Ag nanocrystals due to the tens of picomoles of NaCl was reported for the first time in here. Adscititious role of NaCl was assumed that the chloride ions in NaCl could effectively bind to the {100} facets of fcc metals, boosting the development of the {100} side-facets of STRBs together with the delay of the Ag complex supply. Further detailed characterization of the GC-STRBs are shown in Figure 2. The conductive junction between Au and Ag was formed as width of 21.4 ± 2.1 nm and a length of 1.6 ± 0.3nm in GC-STRBPs. When the amounts of reducing agent and surfactant were considerably decreased to 0.003 M and 0.2%, respectively, GC-SBs were synthesized, with distinct alternating stripes of light and dark contrast in the TEM image in Figure 3. Interestingly, under these conditions, the plasmonic conductive junction between gold and silver had a width of ~9.6 ± 1.1 nm and a length of 9.8 ± 3.1 nm. In contrast to the GC-STRB conditions that generated a thick and short neck junction , the plasmonic properties of GC-SB which has short and long junction were clearly differentiated by its junction geometry. For example, the appearance of the charge transfer plasmon mode in near-infrared region and local-field enhancement were highly dependent on the junction geometry. We further investigated the junction-geometry induced conductance change in GC-S;body structures with the CTP mode in Figure 4. Figure 2a shows a schematic of the transformation pathway from silver nanoplates to the right bipyramid structure. As previously reported, stacking faults or twin plane-like crystal defects parallel to the (111) plane of Ag were observed, indicating that these two structures were crystallographically related. In the presence of PVP or NaCl as a structure-directing agent, silver atoms were preferentially deposited on the (111) facets; consequently, generating the right bipyramid structures. The truncated right bipyramid structures represented the intermediate state between these two structures composed of either mixture of (100) and (111) facets. By analyzing ~80 nanostructures, two different edge lengths and a height, denoted as a, b, and h, were measured to be 60 ± 5 nm, 15 ± 3 nm, and 48 ± 3 nm, respectively, correlated with the SEM and TEM images. The error ranges were explained by the diverse degree of truncation due to the fast reaction kinetics getting completed in 1 min . We emphasized that even though additional NaCl delayed the reaction kinetics, it is still in regime of fast reaction kinetics as similar to the synthetic condition of GC-SP. In Figure 2b, representative TEM image of a GC-STRB (Figure 2b) shows various particle orientations according to its three-dimensional structural features. The two distinct orientations of the GC−STRB, defined as front (i) and lateral (ii) as labeled in Figure 2, were analyzed using Cs−corrected HR−TEM (Cs−TEM). For the front orientation, the GC−STRB was projected along the <100> direction, generating the cubic projection of GC−head in the TEM image. In this orientation, internal differences of contrast in silver body were observed, confirming the three−dimensional structure of the TRB structure. In particular, at this orientation, a connecting junction with a width of 21.4 ± 2.1 nm and a length of 1.6 ± 0.3nm and a ~1 nm gap between the GC and the STRB was clearly observed. It is known that an adenine rich DNA sequence develops a 1−nm gap at the interface between the seed and the secondary metal because of its strong binding affinity to the gold surface. The magnified images of the dashed box indicates a d−spacing of 2.0 Å for adjacent lattice fringes and fast Fourier transform (FFT) patterns that matched well with the {100} planes of face−centered cubic (FCC) Au and Ag. Note that for the face−centered cubic nanostructures, stacking faults or twin planes were only visible at certain orientations and formed in the most closely packed {111} planes. In the lateral orientation, the electron beam aligned along the <110> direction, clearly visualizing the crystalline defects with distinct contrast in the middle of the silver body, as shown by the dashed box 3 in Figure 2c. Uneven stacking faults and twin planes along the <111> directions were confirmed by the HR-TEM image and its corresponding FFT pattern. Notably, previously reported TRBs w consisted of two right tetrahedral structures joined base-to-base symmetrically. However, our STRBP mostly consisted of stacking faults rather than complete twin planes, resulting in asymmetric TRBPs with edges of different lengths. The magnified images of the dashed box 4 and reduced FFT patterns indicated an interplanar spacing of 2.34 Å, which corresponded to the {111} planes of FCC Ag. To visualize its shape and orientation more clearly, a series of tilted TEM images and correlated 3D modeling images were collected by continuous tilting of the z-axis at 15°. The GC-SBs were synthesized with PVP and AA concentrations as low as 0.2% and 0.003 M, respectively (Figure 3a). From the kinetic point of view, reducing amount of AA decreases the number of efficient collisions between the reducing agent and the silver precursor, causing slow reduction of $AgNO_3$. The molar ratio of AA to Ag precursor decreased to ~6.67 compared to 250 under the previous two conditions, which is still in excess amount. Importantly, in our experiment, the GC seed was dispersed in 10 mM Phosphate buffer (10 mM PB, pH 7.4) instead of DIW which has a dual function as stabilize the GC seeds for storage and mild change in pH value by adding the reducing agent. For example, the pH value change was negligible as decreased from 7.4 to

7.0, with final concentration of 0.003M ascorbic acid. Whereas adding same amount of AA turn it to pH value 3.8 in case of dispersion in DIW. As previously reported, the reducing power of AA highly depends on the pH value which had to be increased as raising pH value. We found that the crystal defect-rich silver nanobars were only synthesized at pH 7, with distinct thin (~ 10 nm) and long (~ 10 nm) connecting junction. In Figure 3b, the HR-TEM image shows alternate stripes of light and dark contrast along the <111> direction. The magnified HR-TEM image (Figure 3b-3) taken along the <110> axis clearly confirms a lattice spacing of ~0.24 nm, corresponding to the (111) facets of Ag, and numerous stacking faults on the silver body. As marked by the yellow dashed lines in Figure 3b-2 and -3, the {111} atomic planes were shifted to the <112> direction for most stacking faults due to the dislocation of the atomic layers. Additionally, crystal defects with atomic vacancies were observed in GC-SBs (marked as green boxes). The FFT pattern in Fig 3b-4 shows a spreading spot pattern along the main spots, confirming the mixing of crystal defects. Here, we suggest the following mechanism for the formation of a stacking fault-rich Ag body in GC-SBs with a relatively high pH value and low PVP concentration. As is well known, PVP could effectively bind to the {100} facets of silver nanostructures; further, the {111} facets were poorly passivated.

Hence, newly generated silver atoms were attached on the {111} facets, resulting in the elongation of particles along the <111> direction. Simultaneously, the enhanced reducing power of AA at pH 7, even though the final concentration was 0.003M, led to rapid deposition of these newly generated silver atoms, slightly breaking the ordering attachment of Ag and resulting in stacking fault-rich structures along the <111> direction. Figure 4 a, b presents the time-dependent UV-vis spectra of the GC-STRBs and GC-SBs. As the silver grew on the GC, gradual evolution of plasmon modes with respect to wavelength was observed. The first resonance peak at ~400 nm in Figure 4a and b was caused by the development of Ag, and the intensity of this peak continuously increased. Interestingly, two new plasmon peaks were observed for the GC-STRBs, marked as SBDP and CTP in Figure 4a, whereas no distinct peaks were observed for the GC-SBs in the same wavelength region. The new plasmon peak appearing at 600 nm corresponded to the screened bonding dipole plasmon mode (SBDP). When two nanoparticles are placed next to each other with a nanometer gap, their plasmon modes can interact, resulting in the BDP mode with large localized charge distributions of opposite signs for both nanoparticles. When these particles are connected by a conductive junction, the spectral position of the BDP mode blue shifts due to the screening effect of charge that expelled across the junction, generating a plasmon mode defined as SBDP together with charges accumulating around the junction. In the GC−STRBs, a conductive junction with a width of ~20 nm ensures charge transport across the junction and simultaneously, accompanying 1−nm gap surrounding the junction promoted the capacitive coupling of charges that piled up in the peripheral gap area. The resulting sBDP mode at 600 nm showed a negligible spectral shift with increased intensity as the reaction proceeded. Three−dimensional finite element model (3D FEM) calculations shown in Figure 5 corroborated that a largely enhanced EM−field was formed around the junction at 600 nm, and the simulated spectra for the far−field matched well with the experimental position of SBPD mode. The differences in resonant energy between simulation and experimental data was ~30 nm, which might have been caused by the imperfect matching of the degree of truncation or length parameters in the model. In contrast, in the GC−SBs, the SBDP mode was not well developed in the 600 nm region. It was assumed that the difference in geometry in peripheral junction as the absence of the 1−nm dielectric gap and relatively thin and long junction as ~ 10 nm of each, did not provide the sites required for charge accumulation. The simulated far−field spectrum of the GC−SBs also generated the absence of SBDP mode as same as experiment. Therefore, we can conclude that the geometry of the peripheral junction together with the thickness and length of junction were important to generate the SBDP mode. Next, we focus on the charge transfer plasmon (CTP) mode to study the relationship between junction geometry and its spectral development. During the gradual formation of GC-STRBP, the CTP mode emerged in the low-frequency region, which supported the entire dipolar charge configuration having a net charge because of the conductive junction. The maximum peak position of CTP red shifted with time from 790 nm to above 1100 nm with a gradual increase in linewidth. (figure 5a) With the ~ 20 nm of thick junction, the low impedance of it could facilitate the charge transfer between Au and Ag, clearly generate the CTP mode. Further, the thickness and length of junction dependent conductance was monitored with its geometry in GC-SBs. Interestingly, the CTP mode did not appear during the growth of the silver of GC-SBs. Although the junction was not in the extremely thin regime as previously reported, which did not generate CTP mode, the geometry of junction of GC-SBs as 10 nm of width and length could significantly contribute to the low conductance, interrupting the development of the CTP mode. To confirm these effect, we simulated series of far-field spectra by varying the junction parameters. (figure 5b) Finally, we investigated the SERS properties of GC-STRBs and GC-SBs. It is well known that the interior or inter−particle nanogaps, especially, 1−nm gap in nanostructures ensure a highly enhanced SERS signal owing to the highly enhanced EM field in confined area. Furthermore, the extended cross−section of the gap region plays an important role in generating the extremely enhanced SERS intensity. To examine these relationships in more detail, first, we synthesized GC−STRBs of various sizes, which had a different cross−section of nanometer gap of peripheral junction, by adjusting the concentration of silver precursor as 0.5×, 1×, 1.5×, and 3× of standard conditions. To monitor the SERS signal, Cy3 dye covalently conjugated with DNA at one end was placed in the 1−nm gap. The fingerprint peak of Cy3 at 1197 cm^{-1} was monitored to analyze the quantitative SERS signals using a 3.3−mW power source with a 633−nm laser for an acquisition time of 3 s. Figure 6a shows the correlated TEM images with 0.5×, 1×, 1.5×, and 3× the standard $AgNO_3$ concentration, which obviously led to a gradually increasing gap region. The UV−vis spectra correlated with the TEM images are shown in Figure 5b; distinct spectral changes were observed with increased scattering efficiency of silver with increasing STRB size. (figure 6b) It was clear that the SERS signal became stronger initially by adjusting the added amount of silver precursor to 2 times that under the standard conditions, indicating that enlarged gap dimensions promoted local−

field distribution at 633 nm. (figure 6c) As mentioned before, the highly enhanced EM field at 630 nm was due to the capacitively coupled charges in the nanometer gap region, which were expected to become more distinct as the gap region expanded. However, a continuous increase in body size of GC-STRB weakened the SERS signal even though those particle accompanied an expanding gap region. It is mainly supposed to the spectral shift of near-field resonance caused by variation in the size of the silver body and peripheral junction. Also, Raman signals of Cy3 dyes in the gap could not efficiently penetrate the enlarged silver body with interrupted signal to be detected. Next, we compared the SERS signals of GC-STRBs and GC-SBs which has a different junction geometry.(figure 6d) The analyzed SERS intensities were 48 and 2 times higher than that of the body-less GCs, respectively. As previously mentioned, the local-field distribution enhancement near 633 nm was negligible in the GC-SBs with a long and thin junction geometry. On the contrary, the GC-STRBs could be detected even at a concentration as low as 50 fM and showed good linear correlations with small standard deviations as a function of particle concentration (Figure 6e). These properties of the GC-STRBs, wherein they produced quantitative and strong SERS signals with a high geometrical sensitivity, can be an excellent candidate for sensing applications.

2.4. Conclusions

In summary, we control the stacking faults in secondary metals as Ag by delicately controlling the reaction kinetics of silver reduction which deposited on the DNA-modified GC seeds. Specially, DNA-mediated growth mode changes from FM mode to VW mode (island mode) can increase the total energy of the silver nuclei at the restricted sites of seed, resulting in symmetry breaking by the formation of crystal defects in the silver body. Various kinds of Au-Ag head-body structures as plates (GC-SPs), truncated right bipyramids (GC-SRBPs) and bars (GC-SBs) were synthesized which have different geometries in conductive junction. In the GC-STRB structures, conductive junction with a width of ~20 nm and a length of ~1.5 nm was developed accompanying the formation of 1-nm gap region peripheral junction. On the other hand, GC-SB structures was composed of junction width of around 10 nm and length of ~ 10 nm.

Here, we found that the small changes of conductive junctions as ~ 10 nm to ~ 20 nm regime, greatly affected the junction conductance and thus its optical properties, which determined the development of BPD and CTP modes. Our strategy in designing and synthesizing plasmonic bimetallic structures with the highly precise synthesis of the thick to thin and long to short conductive junction and stacking fault-mediated various silver structures highly opens revenues in studying and utilizing plasmonic nanostructures. The results shown here provide new insights with a highly controllable conductive junction to understand the electronic properties of metal junctions as a conductance by monitoring the optical signals in plasmonic nanostructures.

2.5. References

1. Xia, X.; Zeng, J.; Oetjen, L. K.; Li, Q.; Xia, Y. *J. Am. Chem. Soc.* **2012**, *134* (3), 1793–1801.

2. Lim, D.-K.; Jeon, K.-S.; Hwang, J.-H.; Kim, H.; Kwon, S.; Suh, Y. D.; Nam, J.-M. *Nat. Nanotechnol.* **2011**, *6* (7), 452–460.

3. Romero, I.; Aizpurua, J.; Bryant, G. W.; García De Abajo, F. J. *Opt. Express* **2006**, *14* (21), 9988.

4. Alber, I.; Sigle, W.; Demming-Janssen, F.; Neumann, R.; Trautmann, C.; Van Aken, P. A.; Toimil-Molares, M. E. *ACS Nano* **2012**, *6* (11),9711–9717.

5. Zhang, M.; Large, N.; Koh, A. L.; Cao, Y.; Manjavacas, A.; Sinclair, R.; Nordlander, P.; Wang, S. X. *ACS Nano* **2015**, *9* (9), 9331–9339.

6. Langille, M. R.; Personick, M. L.; Zhang, J.; Mirkin, C. A. *J. Am. Chem.Soc.* **2012**, *134* (35), 14542–14554.

7. Sun, Y.; Foley, J. J.; Peng, S.; Li, Z.; Gray, S. K. *Nano Lett.* **2013**, *13* (8), 3958–3964.

8. Langille, M. R.; Zhang, J.; Personick, M. L.; Li, S.; Mirkin, C. A. *Science.* **2012**, *337* (6097), 954–957.

9. Xia, Y.; Xia, X.; Peng, H. C. *J. Am. Chem. Soc.* **2015**, *137* (25), 7947–7966.

10. Wang, Y.; He, J.; Liu, C.; Chong, W. H.; Chen, H. *Angew. Chemie*

Int. Ed. 2015, *54* (7), 2022–2051.

11. Costi, R.; Saunders, A. E.; Banin, U. *Angew. Chemie – Int. Ed.* 2010, *49* (29), 4878–4897.

12. Lee, J. H.; You, M. H.; Kim, G. H.; Nam, J. M. *Nano Lett.* 2014, *14* (11), 6217–6225.

13. Langille, M. R.; Personick, M. L.; Mirkin, C. A. *Angew. Chemie Int. Ed.* 2013, *52* (52), 13910–13940.

14. Ringe, E.; Duyne, R. P. Van; Marks, L. D. *J. Phys. Chem. C* 2013, *117*, 15859–15870.

15. Wiley, B. J.; Xiong, Y.; Li, Z.; Yin, Y.; Xia, Y. 2006, 10–13.

16. Lu, N.; Chen, W.; Fang, G.; Chen, B.; Yang, K.; Yang, Y.; Wang, Z.; Huang, S.; Li, Y. *Chem. Mater.* 2014, *26* (7), 2453–2459.

17. Zhang, J.; Li, S.; Wu, J.; Schatz, G. C.; Mirkin, C. A. *Angew. Chemie Int. Ed.* 2009, *48* (42), 7787–7791.

18. Liang, H.; Yang, H.; Wang, W.; Li, J.; Xu, H. *J. Am. Chem. Soc.* 2009, *131* (17), 6068–6069.

19. Liang, H.; Zhao, H.; Rossouw, D.; Wang, W.; Xu, H.; Botton, G. A.; Ma, D. *Chem. Mater.* 2012, *24* (12), 2339–2346.

20. Tong, X.; Liang, H.; Liu, Y.; Tan, L.; Ma, D.; Zhao, Y. *Nanoscale* 2015, *7* (19), 8858–8863.

21. Shi, H.; Dong, B.; Wang, W. *Nanoscale* 2012, *4* (20), 6389.

22. Prodan, E. *Science .* 2003, *302* (5644), 419–422.

23. Nordlander, P.; Oubre, C.; Prodan, E.; Li, K.; Stockman, M. I. *Nano Lett.* 2004, *4* (5), 899–903.

24. Willingham, B.; Brandl, D. W.; Nordlander, P. *Appl. Phys. B Lasers Opt.* 2008, *93* (1), 209–216.

25. Mertens, J.; Demetriadou, A.; Bowman, R. W.; Benz, F.; Kleemann, M. E.; Tserkezis, C.; Shi, Y.; Yang, H. Y.; Hess, O.; Aizpurua, J.;Baumberg, J. J. *Nano Lett.* 2016, *16* (9), 5605–5611.

26. Lee, D.; Yoon, S. *J. Phys. Chem. C* 2016, *120* (37), 20642–20650.

27. Fontana, J.; Charipar, N.; Flom, S. R.; Naciri, J.; Piqué, A.; Ratna, B. R. *ACS Photonics* 2016, *3* (5), 904–911.

28. Wen, F.; Zhang, Y.; Gottheim, S.; King, N. S.; Zhang, Y.; Nordlander, P.; Halas, N. J. *ACS Nano* 2015, *9* (6), 6428–6435.

29. Millstone, J. E.; Park, S.; Shuford, K. L.; Qin, L.; Schatz, G. C.; Mirkin, C. A. *J. Am. Chem. Soc.* 2005, *127* (15), 5312–5313.

30. Pérez−González, O.; Zabala, N.; Aizpurua, J. *New J. Phys.* 2011, *13*. 161−163

31. Huang, Y.; Ma, L.; Hou, M.; Xie, Z.; Zhang, Z. *Phys. Chem. Chem. Phys.* 2016, *18* (4), 2319–2323.

32. Duan, H.; Fernandez, A.; Bosman, M.; Maier, S. a; Yang, J. K. W. *Nano Lett.* 2012, 1–9.

33. Koya, A. N.; Lin, J. *J. Appl. Phys.* 2016, *120* (9).

34. Pérez−González, O.; Zabala, N.; Borisov, A. G.; Halas, N. J.;

Nordlander, P.; Aizpurua, J. *Nano Lett.* **2010**, *10* (8), 3090–3095.

35. Nie, S.; Emory, S. R. *Science* 1997, **275**, 1102−1106.

36. Itoh, T.; Yoshida, K.; Biju, V.; Kikkawa, Y.; Ishikawa, M.; Ozaki, Y. *Phys. Rev. B* 2007, **76**, 085405.

37. Yoshida, K.−i.; Itoh, T.; Biju, V.; Ishikawa, M.; Ozaki, Y. *Phys. Rev. B* 2009, **79**, 085419.

38. Schnell, M.; García−Etxarri, A.; Huber, A. J.; Crozier, K.; Aizpurua, J.; Hillenbrand, R. *Nat. Photonics* **2009**, *3* (5), 287–291.

39. Tan, S. J.; Campolongo, M. J.; Luo, D.; Cheng, W. *Nat. Nanotechnol.* 2011, **6**, 268−276.

40. Feng, Y.; Wang, Y.; He, J.; Song, X.; Tay, Y. Y.; Hng, H. H.; Ling, X. Y.; Chen, H. *J. Am. Chem. Soc.* **2015**, *137* (24), 7624–7627.

Figures

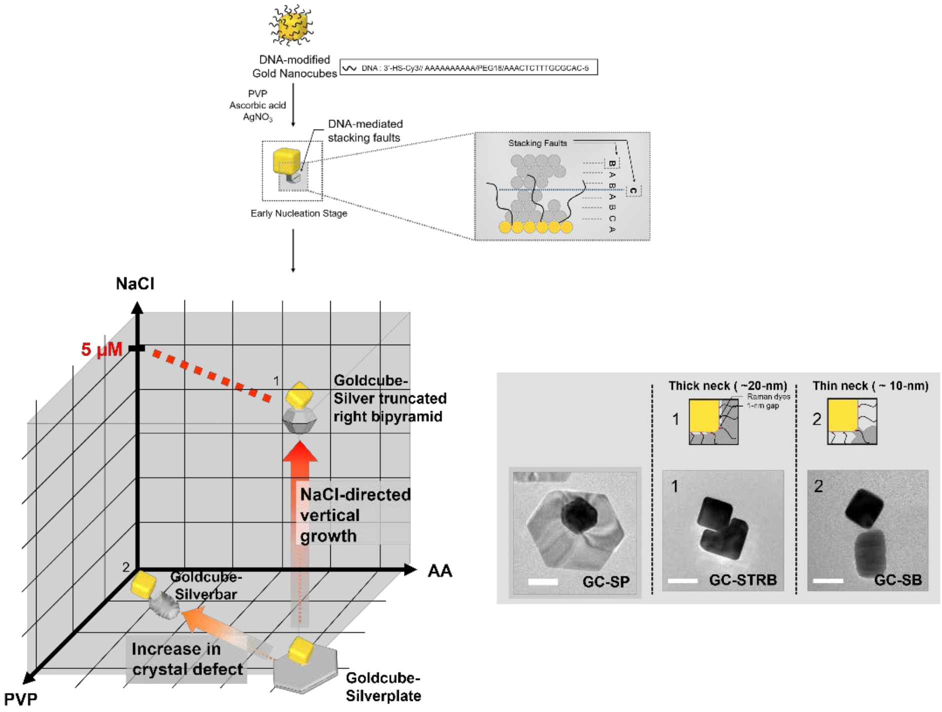

Figure 1. Illustration of scheme for synthesizing various types of Au–Ag hetero dimer structures and transmission electron microscope images of Au;cube–Ag;plate, truncated right bipyramid and bar head–body structures with controlled conductive junctions in various synthetic conditions.

.

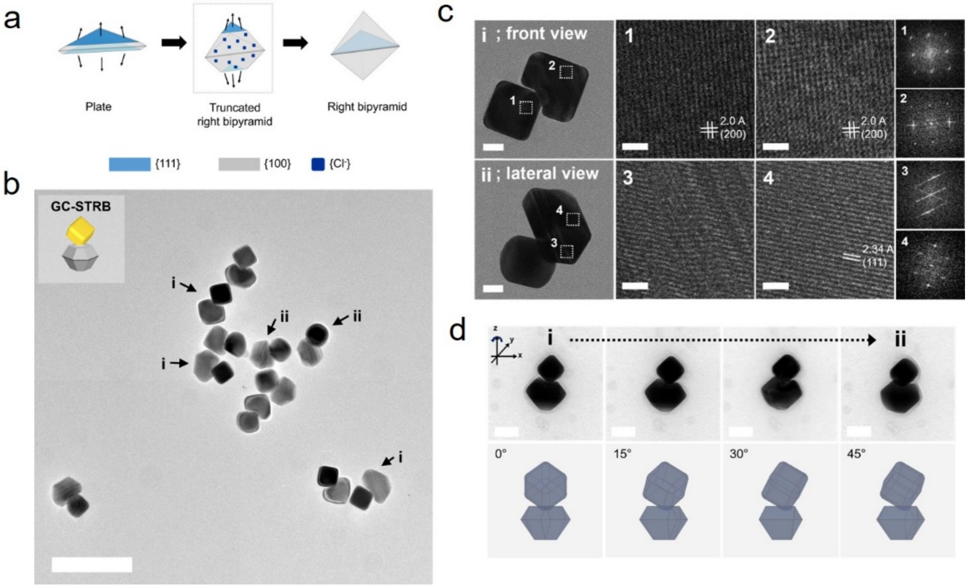

Figure 2. (A) Schematic views of transformation pathway from silver plate to right bipyramid structures. (B) Transmission electron microscope image of GC-STRB structures with low magnitude image. (C) Orientation dependent HAADF-TEM images of GC-STRB from front and lateral view and corresponding FFT patterns marked as box. (D) Series of tilted TEM images and correlated 3D modeling images which were collected by continuous tilting of the z-axis at 15°

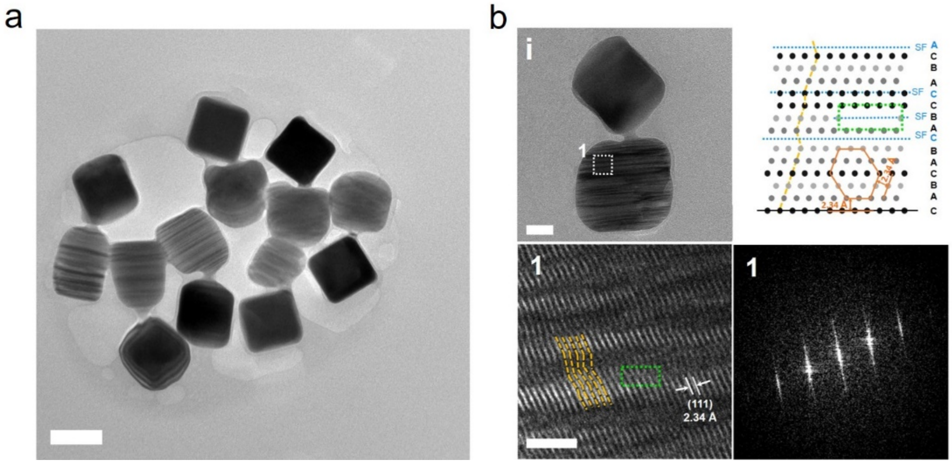

Figure 3. (A) Transmission electron microscope image of GC-SB structures with low magnitude image. (B) Representative single-particle HAADF-TEM images of GC-SB and magnified lattice image in silver body and corresponding FFT patterns from marked as box1.

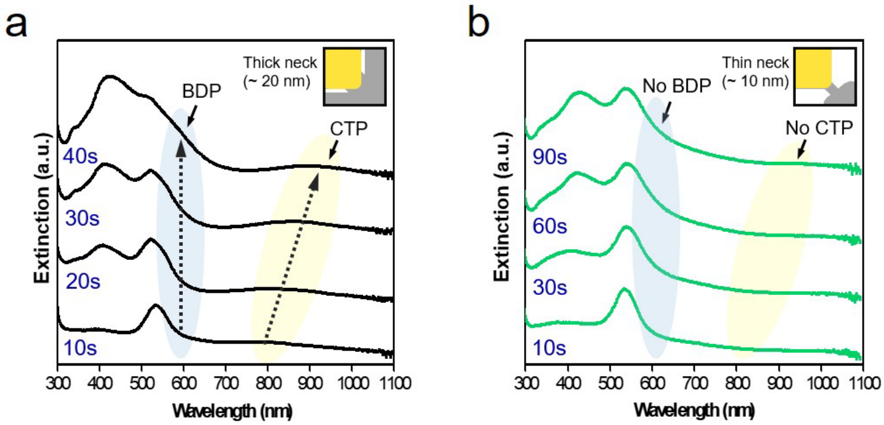

Figure 4. (A) The time-dependent UV-vis extinction spectra of the GC-STRB with continuous development in bonding dipolar plasmon mode and charge-transfer plasmon mode. (B) The time dependent UV-vis extinction spectra of GC-SB with negligible development in both bonding dipolar plasmon mode and charge-transfer plasmon mode.

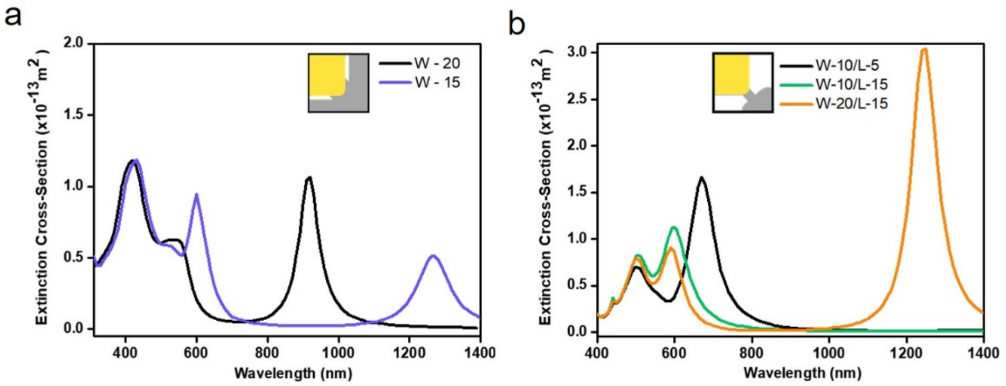

Figure 5. (A) The 3D FEM calculation-based extinction spectra of GC-STRB (thick and short junction, inset) structures with different conductive junction geometries (B) The 3D FEM calculation-based extinction spectra of GC-SB (thin and long junction, inset) structures with different conductive junction geometries

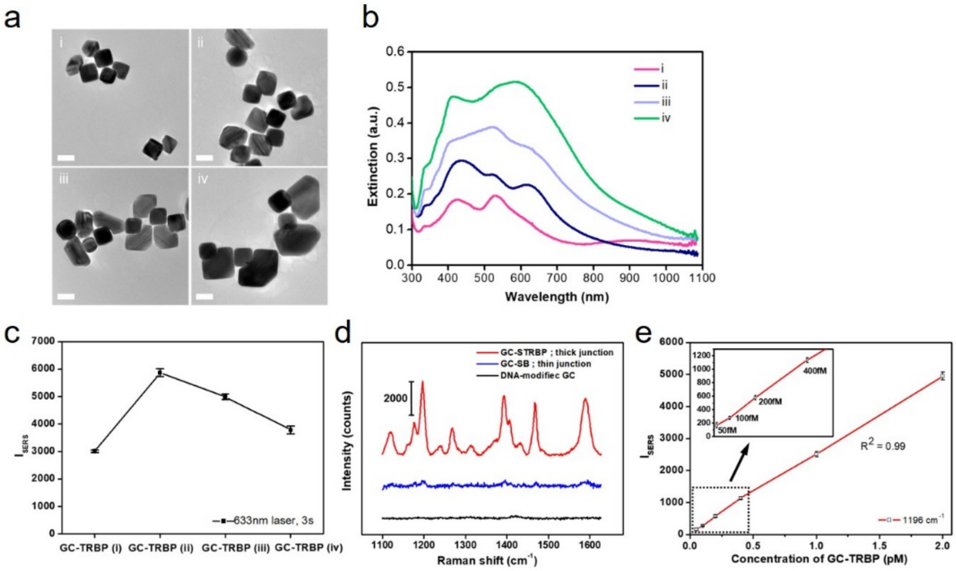

Figure 6. (A) TEM images of GC−STRB structures with different Ag body sizes. All the scale bars are 50 nm in the TEM images. (B) The extinction spectra of GC−STRB structures with different Ag body sizes. (C) Comparison in the SERS intensities between different sizes in GC−STRB structures. (D) Comparison in the SERS intensities between Raman dye modified GC (control) GC−STRB and GC−SB structures. (E) SERS intensity plot at 1198 cm^{-1} of Cy3 dye from GC−STRB structures in Figure 2 as a function of nanoparticle concentration. All the spectra were taken at 633 nm laser with ~3.3 mW laser power, 3 s acquisition time, 20× objective lens, and static mode.

요약(국문초록)

고도로 제어된 금-은 헤드부-바디부로 나노구조체의 합성 및 그 구조에 따른 광학적 특성 연구

금, 은, 구리 등 귀금속으로 이루어진 나노 입자는 금속의 전도대에 풍부하게 존재하는 자유전자로 인해 국소화된 표면 공명 플라즈몬 (Localized Surface Plasmon Resonance, LSPR) 현상을 나타낸다. 외부의 전자기장과 감응하는 이들의 공명 주파수는 금속 나노 입자의 크기, 모양, 구성물질, 외부의 환경 등에 크게 의존하는 특성을 나타내는데 이는 바이오 검지 및 이미징 등의 의료 진단의 영역에서부터 전기, 촉매, 에너지 저장까지 다양한 분야로의 응용 가능성을 내포하고 있다. 현재의 플라즈모닉 나노 구조체에 대한 연구는 다양한 형태의 단일 금속 나노 입자를 균일하게 합성하고 응용하는 수준을 넘어서 이금속 및 다중 금속 등의 새로운 시스템의 개발 및 응용으로 확장되고 있다. 이 중 서로 다른 금속이 하나의 시스템을 이루는 이금속 나노 입자는 각각의 독특한 물리, 화학적 특성의 조합 및 이들의 상호작용으로 인한 시너지 효과로 인해 더욱 다양하고 새로운 특성을 나타낼 수 있다. 특히 이금속 나노입자는 입자 내부에 의도적으로

날카로운 틈을 형성하거나 나노미터의 간극 및 울퉁불퉁한 표면 등을 도입하여 플라즈모닉 커플링 현상을 유도할 수 있고, 이는 나노미터의 거리를 갖고 분리된 이합체 구조에서 나타나는 것과 같은 강력한 전자기장 증폭 효과를 나타내어 라만 산란 및 형광 등의 다양한 분광학적 신호를 증폭시킬 수 있다. 또다른 예로, 서로 다른 두 금속이 아령 형태의 구조로 비등방적으로 연결된 이금속 나노입자의 경우, 분자궤도함수의 혼성화 원리로 설명되는 플라즈몬 혼성 이론에 따라서, 입자 내부의 대칭 깨짐으로 인해 반결합성 플라즈몬 벡터의 합이 0이 아니게 되어 다양한 플라즈몬 모드가 여기될 수 있다는 장점이 있다. 그러나 현재까지 이금속 나노입자의 구조를 정교하게 조절하고 높은 수율로 균일하게 합성하는 것은 구조 자체의 낮은 열역학적 안정도로 인하여 합성에 있어서 근본적인 어려움이 존재한다. 특히 두 금속을 잇는 전도성 정션의 날카로운 정도 및 길이와 두께 등을 정교하고 재현성있게 조절하는 것은 나노 물질의 광학적, 전기적 특성 등의 변화를 나타내기 때문에 매우 중요하며, 많은 연구가 이러한 영역에서 활발히 진행되고 있다.

본 학위 논문에서는 이금속 나노입자의 구조를 정교하게 조절하기 위해 금 나노 입자 위에 DNA가 개질된 시스템을 기반으로 한 다양한 합성 접근 방법과 그로 인한 광학적 특성에 대한 연구 결과들을

소개한다. 개괄적으로는 DNA가 개질된 금 나노입자위에 은 나노입자의 비등방적 성장을 위한 합성법에 대한 연구이며, 특히 반응속도론적인 측면에서 DNA, 환원제의 양, pH, 용액 내 염 (NaCl) 등의 요소를 체계적으로 조절함으로써 입자 내 틈새의 날카로운 정도, 은 나노입자 내부에 형성되는 표면 결함 및 이로 이용한 은 나노입자의 입체적인 구조의 조절 등에 대한 연구를 수행하였다. 나노 및 광학 분야에서 있어서 입자의 전기 전도도, 라만 산란 및 형광 등의 분광학적 신호의 획기적으로 증폭시킬 수 있는 시스템의 개발은 가장 활발하게 연구되고 있는 분야 중 하나이다. 본 학위 논문에서는 입자 내부의 날카로운 접합 영역에서 강하게 증강되는 라만 신호를 기반으로 하여 나노 스노우맨 구조가 바이오 검지에 있어서 초고감도 및 고속 진단법에 활용될 수 있을 것으로 기대한다. 또한 이금속 나노 입자 내부의 전도성 정션의 두께 및 길이 조절을 통한 금속의 전기 전도도에 대한 간접적인 이해가 가능함을 연구하였다.

제 1장에서는 DNA 가 표면에 개질된 구형 금 나노입자 및 용액 내 염 (NaCl) 농도를 조절하여 반응 속도를 섬세하게 조절하고 이를 통해 이차적으로 성장하는 은 나노입자가 접합 영역을 가지고 비등방적으로 성장되게 하였다. 특히 접합 영역의 날카로운 정도를 조절함으로써 전하 이동 플라즈몬 모드 및 축전 플라즈몬 모드가 이러한 구조 변화에 매우

민감하다는 것을 관찰하였고, 접합 영역에서 강하게 증강되는 전자기장을 이용해 표면 증강 라만 산란 신호의 증폭에 있어서 1.3 x 10^6 정도의 증강지수를 확인하였다. 특히 이러한 구조의 재현성있는 높은 합성 수율과 넓은 파장 영역과 감응하는 LSPR 특성 및 민감하고 정량적인 분광학적 신호 생성은 다양한 응용 연구에 적용될 수 있는 가능성을 보여준다.

제 2장에서는 DNA 가 표면에 개질된 큐브 형태의 금 나노입자를 반응의 핵으로 이용하고, 반응속도론적인 요소들을 체계적으로 조절함으로써 은 나노입자가 다양한 입체 구조로 성장할 수 있는 새로운 합성법을 개발하였다. 이는 환원제인 아스코르브산의 첨가 양에 따라 변화하는 용액의 pH와 이로 인한 환원력의 차이를 이용한 방법으로 특히 DNA로 인해 은 전구체가 고체로 환원될 때 수반되는 표면 결합을 기반으로 한 연구이다. 이를 통해 금 나노 큐브와 전도성 정션으로 연결된 이차적인 은의 구조를 판형 구조에서부터 양 끝이 잘린 양추형 구조 및 쌓임 결합이 풍부한 나노 막대 구조까지 다양하게 조절 가능하다는 것을 보였다. 또한 3 장에서 제시된 염의 첨가량보다 약 100 배 감소된 극미량의 염 (NaCl)의 첨가를 통해서 은의 성장 방향을 표면 결합면을 따라 평행하게 성장되는 방향에서 수직 방향으로 전환될 수 있고 이때, 약 1 nm의 나노갭이 금 나노 큐브 주변에 형성됨을

밝혀내었다. 특히 위와 같은 구조들이 공통적으로 갖는 전도성 정션의 두께 및 길이를 조절함으로써 다양한 플라즈몬 모드의 발달을 연구할 수 있었으며, 특히 전하 이동 플라즈몬 모드를 기반으로 하여 전도성 정션을 갖는 나노 입자의 전기 전도도에 대한 연구를 간접적으로 수행할 수 있었다.